bioRxiv preprint doi: https://doi.org/10.1101/265330; this version posted February 14, 2018. The copyright holder for this preprint (which was not certified by peer review) is the author/funder. All rights reserved. No reuse allowed without permission.

Measuring the self-assembly kinetics of individual viral capsids

Rees F. Garmann,[†,¶] Aaron M. Goldfain,[†,¶] and Vinothan N. Manoharan[*,†,‡]

†*Harvard John A. Paulson School of Engineering and Applied Sciences, Harvard University, Cambridge, MA*

‡*Department of Physics, Harvard University, Cambridge, MA*

¶*equal contribution*

E-mail: vnm@seas.harvard.edu

Abstract

Self-assembly is widely used by biological systems to build complex and functional nanoscale structures, but the assembly pathways are difficult to observe because of the small length scales and wide range of time scales involved. We describe a label-free optical method to directly probe the assembly of individual nanostructures, and we apply it to measure the kinetics of assembly of viral capsids 28 nm in diameter and consisting of 90 protein subunits. We use a rigid flow cell to inject a solution of the coat protein of bacteriophage MS2 over multiple MS2 RNA strands that are tethered to a microscope coverslip by specific DNA linkages. Using an interferometric detection scheme, we measure changes in the intensity of light scattered from the proteins while they are assembling around each RNA. The low photodamage afforded by elastic scattering enables high illumination intensities and temporal resolutions down to 1 ms, while 3D-active stabilization of the microscope extends the measurement duration to 600 s or longer. With this wide range of timescales, we find that the assembly is characterized by an exponential distribution of wait times preceding a rapid growth phase,

bioRxiv preprint doi: https://doi.org/10.1101/265330; this version posted February 14, 2018. The copyright holder for this preprint (which was not certified by peer review) is the author/funder. All rights reserved. No reuse allowed without permission.

suggesting that the pathway under the conditions we investigate is nucleation followed by growth. Because the method can measure the assembly of many individual capsids in parallel, from start to finish, it offers a direct view of the self-assembly process not accessible to bulk scattering or spectroscopic techniques. It can be adapted to study the assembly of other viruses, biomolecular assemblies, and synthetic nanostructures.

Introduction

Self-assembly is widely used by biological systems to build complex and functional subcellular structures,[1] but the assembly pathways—the ways in which the system proceeds from a disordered state to an ordered one—are challenging to measure and therefore largely unknown. The classic example of self-assembly in biology, and indeed the very first process to be termed "self-assembly,"[2] is the formation of a viral capsid: the compact and highly ordered protein shell that surrounds the nucleic-acid genome of a virus. The capsids of many small, icosahedral RNA viruses can be assembled *in vitro* simply by mixing together the constituent protein and RNA molecules in the absence of ATP-hydrolysis or host-cell factors.[3–5] These results suggest that capsid assembly is driven by the minimization of free energy. Yet we still do not understand basic features of the assembly pathway, such as whether the rate-limiting step is nucleation, growth, or rearrangement of the proteins following an initial "en masse" attachment.[6,7]

It is not for lack of attention that such questions remain unanswered. The structures of viral capsids, their proteins, and their RNA cargoes have been studied in extraordinary detail through X-ray crystallography and cryo-electron microscopy.[8] But such measurements are currently limited to static snapshots of the structure at a given time, and they reveal only indirect information about how that structure forms. Although the assembly dynamics can be monitored in bulk using light-scattering[9,10] or fluorescence correlation spectroscopy,[11,12] important steps of the assembly process may be obscured in such measurements, which average over an ensemble of particles in possibly different stages of growth. More recently,

bioRxiv preprint doi: https://doi.org/10.1101/265330; this version posted February 14, 2018. The copyright holder for this preprint (which was not certified by peer review) is the author/funder. All rights reserved. No reuse allowed without permission.

specialized nano-fluidic devices[13,14] have been brought to bear on the problem. Still, no technique has quantified the kinetics of self-assembly at the scale of individual viral capsids.

The challenge in measuring the assembly kinetics of individual capsids lies not only in the length scales involved, which are below the resolution limit of optical techniques, but also in the time scales. Bulk kinetic studies suggest that capsid assembly around RNA might take anywhere from milliseconds to many minutes to complete.[11,15] The enormous uncertainty in the time scales is partly due to the assembly pathway being unknown. For example, if assembly follows a nucleation-and-growth pathway, the proteins might take a long time to form a critical nucleus but a short time to form a capsid once nucleation occurs. Thus, an experiment must be able to image the assemblies with high temporal resolution (sub-second) over long durations (hundreds of seconds). This broad dynamic range is difficult to achieve in many biological imaging techniques.

Here we show that an elastic light-scattering method called interferometric scattering microscopy,[16] in conjunction with active three-dimensional (3D) stabilization and a rigid flow cell, can measure the kinetics of assembly of individual capsids around RNA molecules that are specifically tethered to a functionalized surface. Although interferometric scattering has been used to monitor the assembly of supported lipid bilayers[17] and the disassembly of individual microtubules,[18] these systems are much larger than small RNA viruses, and they span many micrometers in at least one dimension. One can extract the kinetics of such a system by measuring the size of its image as a function of time. By contrast, a capsid is much smaller than the wavelength of light, and so the extent of its image does not change appreciably during assembly. We therefore measure the size of an assembling capsid through changes in the amount of light that it scatters (see Figure **1**). Because the scattering is elastic, high illumination intensities can be used with minimal risk of photodamage, enabling temporal resolutions down to 1 ms. To simultaneously achieve durations of up to 600 s, we actively stabilize the microscope in all three dimensions to minimize mechanical drift, which, if left uncorrected, would lead to large variations in intensity over time. Thus, the technique

bioRxiv preprint doi: https://doi.org/10.1101/265330; this version posted February 14, 2018. The copyright holder for this preprint (which was not certified by peer review) is the author/funder. All rights reserved. No reuse allowed without permission.

is able to measure changes in the size of an individual capsid over time scales spanning nearly six orders of magnitude.

We demonstrate the capabilities of this method by measuring the *in vitro* assembly kinetics of bacteriophage MS2, a positive-sense RNA virus with a capsid about 28 nm in diameter.[19] We choose MS2 because its structural[20,21] and biochemical properties[22] are well characterized, but its assembly pathways are not completely understood. MS2 virus-like particles assembled *in vitro*—that is, without the maturation protein required for infectivity—contain 90 dimers of the coat protein (13.7 kDa) arranged with $T = 3$ symmetry,[23] meaning that the coat proteins cannot all be in equivalent local arrangements. How the proteins assemble into the proper quasi-equivalent[2] configurations required to form the complete capsid is a longstanding question, with some suggesting that specific interactions with the RNA are crucial.[24,25] We therefore do all of our measurements with the native MS2 RNA.

Our results show that for the conditions used in our experiments, the assembly pathway for MS2 capsids is nucleation followed by growth. We are able to distinguish this pathway from other possible ones by monitoring the assembly as a function of time for multiple individual capsids in parallel. The method therefore reveals previously unseen features of a process that is critical to viral replication. We expect that it can be adapted to study the kinetics of assembly of many different complex nanoscale structures that are built from large numbers of subunits, including other ribonucleoprotein assemblies,[26] DNA nanostructures,[27] and nanoparticle assemblies.[28]

Results

Measurement overview

Our method takes advantage of a well-established protocol for *in vitro* assembly of MS2 capsids.[4] In this protocol, MS2 coat proteins are first purified from the virus (Supplementary Figure **1**) and then equilibrated in acidic solution, where they form stable dimers. Then the

bioRxiv preprint doi: https://doi.org/10.1101/265330; this version posted February 14, 2018. The copyright holder for this preprint (which was not certified by peer review) is the author/funder. All rights reserved. No reuse allowed without permission.

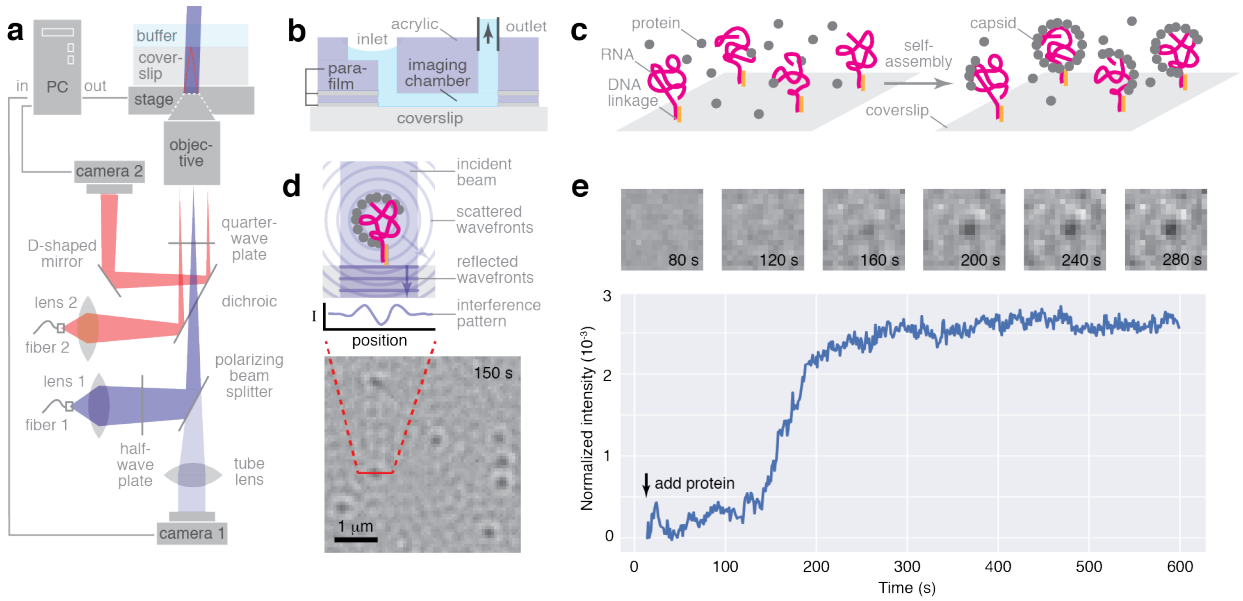

Figure 1: An overview of the method. (a) A diagram of the interferometric scattering microscope. (b) A rigid flow cell is used to introduce the MS2 coat proteins. (c) The proteins self-assemble around viral RNA molecules that are tethered to a coverslip by DNA linkages. (d) As the assemblies grow, they scatter more light. The pattern of interference between the scattered light and the reflection from the coverslip-water interface is imaged onto a camera. The image reveals several assemblies recorded 150 s after introducing 2 μM of coat-protein dimers. The assemblies appear as dark spots, owing to destructive interference between the scattered and reflected light. For clarity, the image is cropped to show only a portion of the total field of view. (e) A time-series of images that have been further cropped to show a single assembly. Below the images is a plot of the normalized intensity of the assembly as a function of time. Details of the experiment that produce the data in (d) and (e) are described in the text.

bioRxiv preprint doi: https://doi.org/10.1101/265330; this version posted February 14, 2018. The copyright holder for this preprint (which was not certified by peer review) is the author/funder. All rights reserved. No reuse allowed without permission.

dimers are mixed with RNA in bulk solution at neutral pH and moderate salt, where they assemble into $T = 3$ capsids that package the RNA (Supplementary Figure **2**). The *in vitro*-assembled capsids have the same structure as the *wild-type* virus, except that they have a coat-protein dimer in place of the maturation protein.[21]

We modify this protocol so that we can directly image the assembling capsids using the apparatus shown in Figure **1**a. We inject a solution of MS2 coat-protein dimers through a rigid flow cell (Figure **1**b) and into an imaging chamber containing MS2 RNA strands that are tethered to the surface of a coverslip (Figure **1**c). We then record, as a function of time, the pattern of interference between light that is reflected from the coverslip surface and light that is backscattered from assemblies of coat proteins near the same surface (Figure **1**d, cartoon). In a typical experiment, multiple diffraction-limited spots appear within the field of view, each of which represents an individual assembly (Figure **1**d, image). We show one of these spots and its intensity as a function of time in Figure **1**e.

Although the images do not reveal the structures of the assemblies, the intensity of each spot is proportional to the number of coat proteins within it. The proportionality follows from the way the image is formed: The intensity of a spot is $I = I_\mathrm{r} + I_\mathrm{s} + 2\sqrt{I_\mathrm{r} I_\mathrm{s}} \cos \phi_\mathrm{rs}$, where I_r is the intensity of the reference (or, equivalently, the reflected) wave, I_s the intensity of the scattered wave, and ϕ_rs the phase difference between the two. For small particles, I_s is small compared to I_r. Therefore, to a good approximation, the normalized intensity $I_\mathrm{norm} = I/I_\mathrm{r} - 1$ is proportional to $\sqrt{I_\mathrm{s}}$, which, for homogeneous, subwavelength particles, is directly proportional to the particle's polarizability.[29] For the inhomogeneous MS2 assemblies we study here, the total polarizability is approximately the sum of a protein component, which is proportional to the volume or number of coat proteins in the assembly, and an RNA component, which is constant. We previously showed that this linear superposition is a good approximation for bacteriophage λ particles, which consist of a protein capsid surrounding a single molecule of densely packed DNA.[30] The interferometric method therefore gives a sensitive measure of the size of an assembly.

bioRxiv preprint doi: https://doi.org/10.1101/265330; this version posted February 14, 2018. The copyright holder for this preprint (which was not certified by peer review) is the author/funder. All rights reserved. No reuse allowed without permission.

However, measuring the assembly of individual capsids from start to finish entails several technical challenges. First, we must correct for even slight drift of the coverslip relative to the objective, which can cause large fluctuations in the background intensity and obscure the kinetics at the late stages of assembly. We apply active stabilization to reduce the drift and minimize background fluctuations. As in previous setups,[31] we measure the position of the coverslip along the dimension perpendicular to its surface using a totally internally reflected beam (red in Figure 1a), and we correct for drift using a proportional control loop that adjusts the height of a piezoelectric stage. But, in contrast to previous setups, we also measure the in-plane position by tracking the image of a gold nanoparticle that is adsorbed to the coverslip, and we correct for drift by moving the stage. This 3D, active stabilization approach maintains the initial position of the coverslip to within a few nanometers in all three dimensions for tens of minutes (Supplementary Figure 3), enabling precise measurements of particle intensities for long times.

Second, we must minimize background fluctuations caused by injecting the coat protein into the imaging chamber. While relatively short-lived, the fluctuations are not mitigated by our active stabilization routine and can easily overwhelm the signal in the early stages of assembly. Because the fluctuations result from warping of the coverslip, we minimize them by attaching a rigid flow cell, as shown in Figure 1b and Supplementary Figure 4. The coat-protein solution flows through millimeter-scale chambers in the cell and then over the RNA molecules bound to the coverslip. The parabolic flow profile[32] within the chamber prevents the surface-bound RNA strands from being immediately immersed by the full concentration of protein. Instead, the protein concentration near the RNA gradually increases as the dimers diffuse from the bulk to the surface. The diffusion of coat-protein dimers to the RNA molecules provides time for any background fluctuations resulting from injection to dissipate before the assembly begins.

Third, the tethering of the RNA to the coverslip must allow for proper assembly. We use specific DNA linkages consisting of a bifunctional DNA oligonucleotide ("linker oligo" in

bioRxiv preprint doi: https://doi.org/10.1101/265330; this version posted February 14, 2018. The copyright holder for this preprint (which was not certified by peer review) is the author/funder. All rights reserved. No reuse allowed without permission.

Figure 2a) that hybridizes to the 5'-end of the RNA and to a second DNA oligonucleotide ("surface oligo") that is covalently bound to the surface.[33] To determine if proper MS2 capsids assemble around such surface-tethered RNA, we use negatively stained transmission electron microscopy (TEM) to image assemblies of coat-protein dimers on RNA molecules that are tethered to gold nanoparticles by the same DNA linkages. The nanoparticles are functionalized similarly to the coverslips, which cannot be imaged using standard TEM methods. A representative micrograph of the assemblies is shown in Figure 2b, and additional micrographs are shown in Supplementary Figure 5. Although some of the assemblies appear incomplete or misshaped, most appear to be well-formed capsids with a roughly spherical shape and a radius consistent with a $T = 3$ structure. The amount of proper capsids relative to malformed structures is qualitatively similar to what we observe in bulk assemblies, though the limited resolution of the TEM micrographs make quantitative comparison difficult.

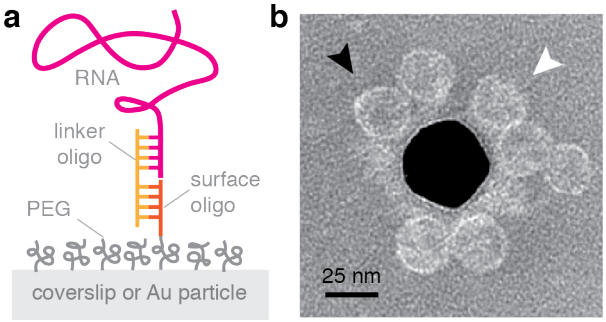

Figure 2: A DNA linkage tethers the viral RNA to the glass coverslip, thereby localizing capsid assembly. (a) A cartoon of the DNA linkage that tethers the viral RNA to the surface. To construct the linkages, we first passivate the surface with a layer of covalently bound polyethylene glycol (PEG). Then we attach the surface oligo to 1% of the PEG molecules. We thermally anneal the RNA to the linker oligo in bulk, and we add the RNA-DNA complexes to the functionalized surface, to which they readily bind at room temperature (Supplementary Figure 6). (b) A negatively stained TEM micrograph of the products of an assembly reaction between MS2 coat proteins and RNA molecules that are tethered by DNA linkages to the surface of a 30-nm gold particle. The black arrowhead points to a well-formed capsid, and the white arrowhead points to a malformed or partially-formed structure.

bioRxiv preprint doi: https://doi.org/10.1101/265330; this version posted February 14, 2018. The copyright holder for this preprint (which was not certified by peer review) is the author/funder. All rights reserved. No reuse allowed without permission.

Dynamic measurements of assembly

We calibrate our interferometric scattering microscope by measuring the normalized intensity distributions of two standards: *wild-type* MS2 particles and bare MS2 RNA molecules. To estimate the range of intensities for capsids that fully assemble during our measurement, we subtract the median intensity of the RNA from the distribution of intensities of *wild-type* MS2 (Figure **3**). The subtraction accounts for the continuous background correction in our measurement (see Methods), which renders static features, like the tethered RNA, invisible. The resulting distribution is peaked at 0.0029, with 90% of the intensities falling between 0.0022 and 0.0036. The shot noise of the measurement is 0.001 (corresponding to 30 coat-protein dimers) per frame, and 0.00003 (1 dimer) after averaging 1,000 frames. The distribution is wider than that expected from shot noise alone because of background fluctuations and uncertainties in locating the centers of the images of particles.

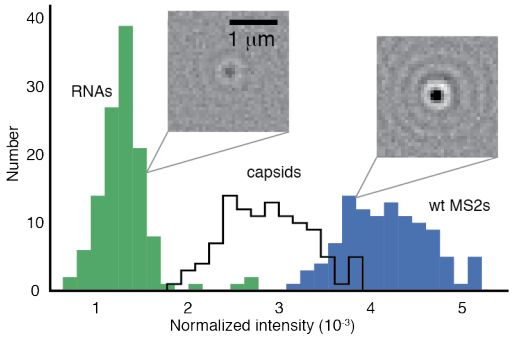

Figure 3: A histogram of the normalized intensities of MS2 RNA and *wild-type* MS2 virus particles measured in our apparatus. We also show the inferred intensity distribution of MS2 capsids that fully assemble during a measurement. The insets show images of a single MS2 RNA molecule (left) and a single MS2 virus particle (right) taken in the microscope. The images and intensities are normalized by dividing the image of the particle by an image of the reflection from the coverslip (see Methods). Both images are recorded at 100 Hz and shown with a 300-frame average.

With the microscope calibrated, we perform the assembly experiment. We inject the RNA-DNA complexes, wait for 10–100 of them to bind to the coverslip, and then rinse

bioRxiv preprint doi: https://doi.org/10.1101/265330; this version posted February 14, 2018. The copyright holder for this preprint (which was not certified by peer review) is the author/funder. All rights reserved. No reuse allowed without permission.

with buffer to remove the unbound ones. We then start recording images and inject known concentrations of coat-protein dimers in assembly buffer (42 mM Tris-HCl, pH 7.5; 84 mM NaCl; 3 mM acetic acid; 1 mM EDTA). When we introduce 1 μM of dimers, we see little change in intensity over the 10 min duration of the experiment (see Supplementary Figure **7**, Supplementary Movie 1). However, when we inject 2 μM of dimers, we observe individual spots growing in intensity after about 1 min (Figure **4**a, Supplementary Movie 2).

The spots do not grow in synchrony, but instead appear after different wait times. The cumulative distribution of wait times—that is, the number of spots N that have appeared at each time point of the movie—is shown in Figure **4**b. We find that the data are well fit by the exponential function $A\left(1-\exp\left[-(t-t_0)/\tau\right]\right)$ (Figure **4**b), where t is time, A is the plateau value, t_0 is the delay before the appearance of the first spot, and τ is the characteristic time. The best-fit parameters are $A = 56.62 \pm 0.02$, $t_0 = 91.8 \pm 0.2$ s, and $\tau = 84.3 \pm 0.2$ s (see Supplementary Figure **8** and the Supplementary Notes for details of the fit).

The intensities of the spots eventually plateau, as shown in Figure **4**c. Out of 56 spots, about half ($N = 25$) have a final intensity that is consistent with that of a full capsid—that is, a final intensity value between the 5th and 95th percentiles of the capsid distribution shown in Figure **3** (see the Supplementary Notes for details of how each spot is located). Some of the spots ($N = 19$) have final intensities that are slightly smaller than that of a full capsid, and others ($N = 12$) have significantly larger intensities. Many of the intensity plots are S-shaped, though some show additional plateaus. Most of the spots reaching high final intensities have intermediate plateaus with intensities consistent with those of full capsids.

Because the number of spots is consistent with the number of tethered RNA molecules, and because sharp increases in intensity do not occur in control experiments without the RNA (Supplementary Figure **10**, Supplementary Movie 3), the spots must result from coat proteins assembling on the tethered RNA. We therefore use the term "growth curve" to describe the intensity of an individual spot—or, equivalently, an assembly—as a function of time. Furthermore, because the intensity scales linearly with the number of proteins,

bioRxiv preprint doi: https://doi.org/10.1101/265330; this version posted February 14, 2018. The copyright holder for this preprint (which was not certified by peer review) is the author/funder. All rights reserved. No reuse allowed without permission.

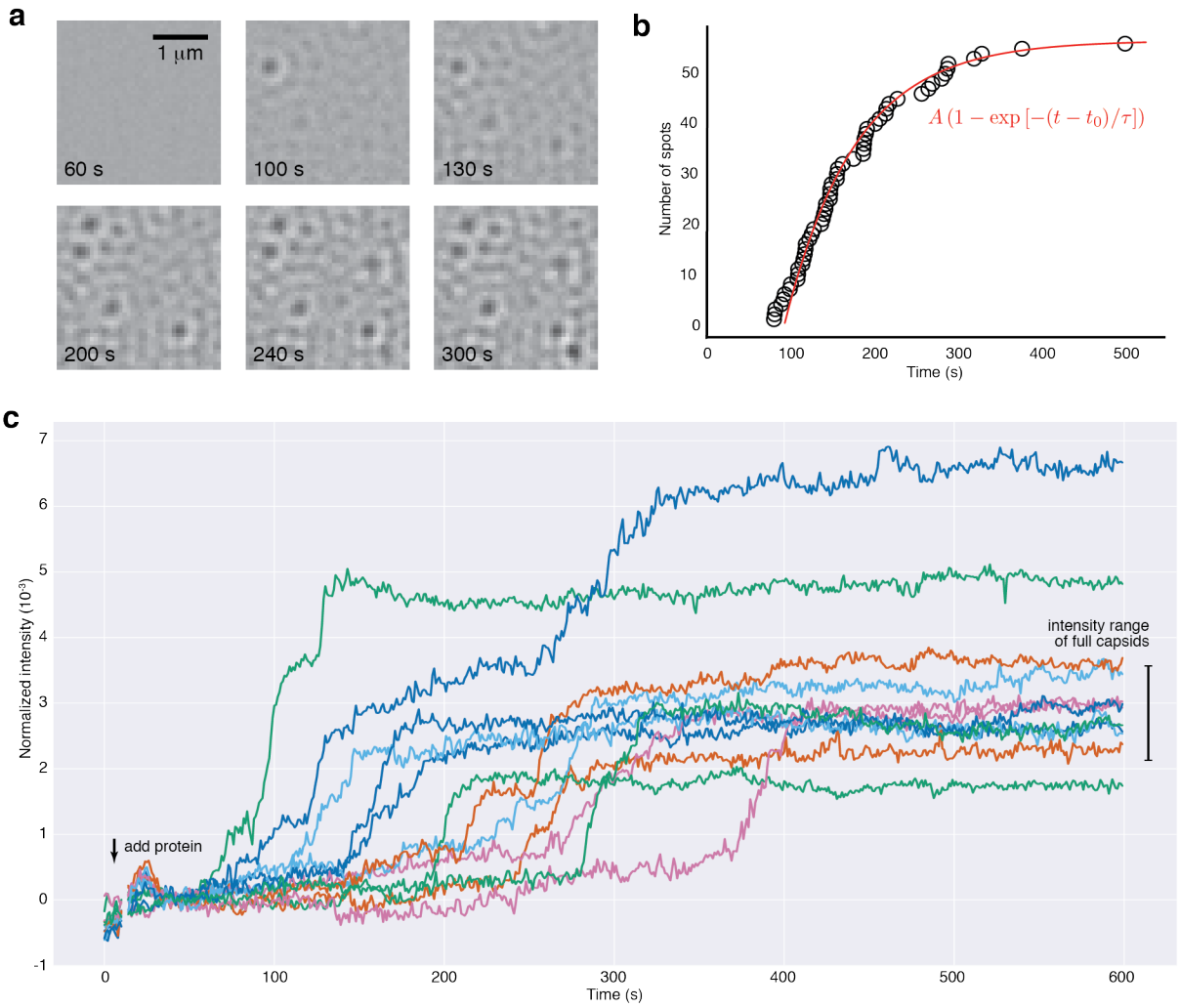

Figure 4: Assembly of 2 μM coat-protein dimers around surface-tethered RNA molecules. (a) A time-series of images of the assembly process from the interferometric scattering microscope. For clarity, we show only a small fraction of the full field of view, and we remove static background features by subtracting off an image taken moments before the first spot appears. The assemblies appear as round dark spots, and the other fainter patterns arise from mechanical drift. (b) The cumulative distribution of wait times that precede assembly is determined by counting the number of spots in the full field of view as a function of time. The maximum uncertainty in the time measurements is represented by the diameter of the circles (see Supplementary Notes for details of the uncertainty analysis). An exponential function is fit to the data as described in the text. (c) The intensity of 12 randomly chosen spots out of a total of 56 from the full field of view as a function of time (the remaining measurements are included in Supplementary Figure 9). The vertical bar shows the expected intensity of a full capsid, as described in the text. The images and extracted intensities are measured at 1,000 Hz and shown with a 1,000-frame average.

bioRxiv preprint doi: https://doi.org/10.1101/265330; this version posted February 14, 2018. The copyright holder for this preprint (which was not certified by peer review) is the author/funder. All rights reserved. No reuse allowed without permission.

each growth curve describes the size of the assembling structure. Indeed, as in our TEM experiments, the range of final sizes extends from about half to twice that of a *wild-type* capsid. We therefore argue that a growth curve plateauing to an intensity consistent with that of a *wild-type* capsid reveals the assembly kinetics of an individual, properly formed capsid.

The delay time preceding the appearance of the first spot likely represents the time for the protein concentration near the coverslip to reach a threshold for assembly. The existence of such a threshold is evidenced by the absence of assembly when we inject 1 μM of coat-protein dimers and its presence with 2 μM. Given the flow velocity and duration, the dimensions of the chamber, and the hydrodynamic radius of a coat-protein dimer ($R_h = 2.5$ nm),[11] the time for diffusion to the surface is approximately 30-55 s (see Supplementary Figure **11** and the Supplementary Notes), which is of the same order of magnitude as the observed delay time.

The wait times after the initial delay, however, likely do not result from a diffusion-limited process. The wait times are broadly distributed, with the largest time extending to nearly 500 s, an order of magnitude larger than the time for protein to diffuse to the surface. We would expect the observed wait times to result from diffusion-limited growth only if there were large differences in the local protein concentration surrounding each RNA within the field of view of the microscope. However, the time for a coat-protein dimer to diffuse across the 10 μm × 10 μm field of view is only 1 s, much shorter than the median wait time. Furthermore, following the initial delay time, there are on the order of 1,000 dimers within a micrometer of each RNA. Therefore, the local concentration is large enough that the relative fluctuations are small, and the pool of dimers available for assembly is not significantly depleted by the growth process. We conclude that the observed growth curves do not result from differences in the local protein concentration around each RNA.

Instead, the data suggest that the assembly pathway involves a free-energy barrier associated with nucleation. While nucleation models have been used to describe the bulk assembly

bioRxiv preprint doi: https://doi.org/10.1101/265330; this version posted February 14, 2018. The copyright holder for this preprint (which was not certified by peer review) is the author/funder. All rights reserved. No reuse allowed without permission.

kinetics of empty capsids,[9,10,34] and computer simulations have explored nucleated pathways for capsid assembly around RNA,[6,7,35] direct evidence for nucleation has remained elusive. Our measurements of the assembly kinetics of multiple individual capsids at the same protein concentration provide this direct evidence: the growth curves show a distribution of wait times that is much wider than that expected from concentration fluctuations alone. That the cumulative distribution of wait times is fit well by an exponential function suggests a well-defined free-energy barrier to nucleation, though further experiments are needed to determine whether the nucleation follows a classical pathway and, if so, what the critical nucleus size is.

The growth curves contain information about the entire assembly pathway, and not just the nucleation step. While most of the curves for proper capsids show a characteristic S-shape, the slope of the growth phase can vary between assemblies, and some of the assemblies show additional plateaus, indicating that each capsid may not assemble by the same set of steps. Curves that plateau to sizes smaller than a complete capsid likely represent incomplete assemblies. Such malformed or partially formed structures could result from interactions with the surface or DNA-linkage or might represent kinetic traps inherent to the assembly process.[36] The curves that tend to larger values might result either from separate assembly events occurring on different RNA strands near one another (within the approximately 160-nm resolution of the microscope) or from the formation of aberrant structures that are larger than a single capsid.[37] However, it is intriguing that most of the assemblies that grow to large intensities show an intermediate plateau, suggesting that these assemblies may have undergone a second nucleation event. Such doubly-nucleated pathways may be responsible for the formation of "monster"[38] and "multiplet"[5,39,40] structures that have been observed with other viruses.

To test whether the illumination intensity affects the assembly process, we perform control experiments in which the imaging beam intensity is decreased by an order of magnitude. These experiments show similar kinetics (Supplementary Figures **12**, **13**; Supplementary

bioRxiv preprint doi: https://doi.org/10.1101/265330; this version posted February 14, 2018. The copyright holder for this preprint (which was not certified by peer review) is the author/funder. All rights reserved. No reuse allowed without permission.

Movies 4, 5; Supplementary Notes). Although the median wait times differ from experiment to experiment (Supplementary Figure **14**), there is no evidence that they depend on the illumination intensity.

Discussion

By following many individual assemblies in parallel over a broad range of time scales, our method opens a new window onto self-assembly at the nanoscale. We have illustrated this point with measurements of viral capsid assembly showing that the pathway—under the *in vitro* conditions we examine—is nucleation followed by growth. The evidence for this pathway, such as the distribution of wait times, is difficult to obtain in other techniques used to examine viral self-assembly. Bulk light scattering techniques[9,10] measure the intensity of an ensemble of assemblies, not all of which are in the same stage of growth. Inferring the assembly pathway from such measurements requires fitting theoretical models[10,41] to subtle features in the data.[42,43] Time-resolved small-angle X-ray scattering[15,44] and fluorescence correlation spectroscopy[11,12] provide additional structural information that can been used to infer assembly intermediates, but these techniques also sum or average the signals from different structures. Finally, approaches such as resistive-pulse sensing[14] and time-resolved negatively stained TEM,[45] can detect individual growing capsids but do not follow the same assemblies throughout the experiment.

Fluorescence microscopy has been used to resolve the biogenesis of individual HIV-1 virus-like particles in live cells by recording the colocalization of fluorescently labeled viral proteins and RNA.[46] These measurements resolve the sequence by which viral subunits associate with one another, but they address a different problem than the one we study here. The biogenesis of HIV-1 particles is determined by active processes within the host cell and interactions with its components, such as the lipid membrane. By contrast, the problem we study, self-assembly, is a physical process driven by thermal fluctuations and

bioRxiv preprint doi: https://doi.org/10.1101/265330; this version posted February 14, 2018. The copyright holder for this preprint (which was not certified by peer review) is the author/funder. All rights reserved. No reuse allowed without permission.

interactions among the coat proteins and the RNA genome. Because the two methods are designed to study different phenomena, they differ in their sensitivities as well: Whereas it is difficult to obtain quantitative measurements of the number of fluorescently-labeled subunits within each HIV-1 particle,[46] our method yields a quantitative measure of the size of the assembling structure. Finally, whereas studying biogenesis in the cell requires fluorophores to distinguish viral components from cellular ones, studying self-assembly does not. Our method is label-free, so that it can be used for systems that are not amenable to labeling with fluorescent tags.

Our experiments focus on MS2 assembly for two reasons. First, the capsid is very small (2.5 MDa in mass and 28 nm in diameter). That the method can succesfully probe the assembly pathways of such a small system bodes well for future studies of other viruses and nanostructures. Second, MS2 is a model system for understanding how specific molecular interactions shape assembly pathways and produce complex structures efficiently. A fundamental question in virology is whether specific RNA sequences or local RNA folds control the assembly process.[47,48] Although the viral RNA we use is thermally denatured and then reannealed before use—and may therefore contain unnatural folds—it is possible to perform identical measurements using RNA molecules with different sequences or annealing histories to elucidate how RNA sequence and structure affect assembly. Furthermore, systematic measurements of the kinetics as a function of coat-protein concentration, buffer composition, and temperature will inform new quantitative models of the entire assembly process—including the ways in which assembly fails.

As we have shown, the ability to address a wide range of timescales is crucial for resolving nucleation events. Indeed, the method is well-suited for probing many different kinds of heterogeneous nucleation processes, owing not only to its broad dynamic range, but also to the ability to localize nucleation to specific sites on the coverslip using DNA linkages. Such linkages can be modified to attach many other molecules and particles,[49] making it possible to measure the nucleation kinetics involved in the assembly of other ribonucleoprotein

bioRxiv preprint doi: https://doi.org/10.1101/265330; this version posted February 14, 2018. The copyright holder for this preprint (which was not certified by peer review) is the author/funder. All rights reserved. No reuse allowed without permission.

complexes[26] and DNA nanostructures,[27] as well as in the synthesis of nanoparticles.[50,51]

Methods

Interferometric scattering microscope

Our microscope is configured in wide-field mode—that is, we do not scan the incident beam—and is similar to the setup described by Ortega-Arroyo and coworkers.[31] A 450 nm, 100 mW, single-mode diode laser (PD-01251, Lasertack) is used for illumination. The current driving the laser is modulated with a square wave at a frequency of 1 MHz to decrease the coherence of the laser and limit intensity variations in the background.[52] The beam (shown in blue in Figure 1a) is spatially filtered by a polarization-maintaining single-mode optical fiber (fiber 1; PM-S405-XP, Thorlabs). The filtered light is collected by a lens (lens 1; achromatic doublet, focal length = 25 mm, Thorlabs), reflected from a polarizing beamsplitter cube (Thorlabs), and focused onto the back aperture of the objective (100× oil-immersion, 1.45 NA Plan Apo λ, Nikon) to produce collimated illumination in the imaging chamber. The light that is backscattered from the sample and light that is reflected from the water-coverslip interface is collected by the objective and imaged onto camera 1 (MV1-D1024E-160-CL, Photon Focus) by the tube lens (achromatic doublet, focal length = 300 mm, Thorlabs). We use achromatic half and quarter-wave plates (Bolder Vision Optik) with the polarizing beamsplitter to make an optical isolator that minimizes the intensity lost at the beamsplitter. The total magnification is 150×, such that each pixel on the camera views a field of 70 nm.

The illumination intensity, approximately 3 kW/cm^2 when we record data at 1,000 Hz and 0.3 kW/cm^2 at 100 Hz, is similar to that typically used in single-molecule fluorescence experiments.[53] The total field of view is 140 pixels × 140 pixels (9.8 μm × 9.8 μm) at 1,000 Hz and 200 pixels × 200 pixels (14 μm × 14 μm) at 100 Hz. To minimize any possible radiation damage, we use an exposure time that is almost equal to the total time between frames, and we dim the imaging beam with absorptive filters before it enters fiber 1 so that

bioRxiv preprint doi: https://doi.org/10.1101/265330; this version posted February 14, 2018. The copyright holder for this preprint (which was not certified by peer review) is the author/funder. All rights reserved. No reuse allowed without permission.

the camera pixels are nearly saturated.

The imaging beam is slightly misaligned to reduce back-reflections from the objective and the roof of the imaging chamber. To keep the point-spread function of the microscope symmetric, we set the misalignment as small as possible such that back-reflections from the objective do not overlap with the reference beam on the camera. To accomplish this, we first align the imaging beam with the microscope axis, and then we offset fiber 1 laterally using a two-axis linear translation stage (Thorlabs) and tilt the imaging beam using a mirror mounted in a two-axis kinematic mount (Thorlabs) located between lens 1 and the half-wave plate.

We use short-wavelength light ($\lambda = 450$ nm) because the intensity of the image scales with λ^{-2}. While shorter wavelength lasers are available, we find they can damage both the sample and optical components when used at high intensities.

To minimize vibrations and long-term mechanical drift, we make the imaging beam path as short as possible, we mount the apparatus on an isolated optical table (RS4000, Newport), and we secure all cables going to non-isolated equipment using clamps that we line with semi-rigid foam (0.75-in-thick polyethylene; 8865K522, McMaster-Carr). To minimize thermal drift and the effects of air currents, we cover the entire apparatus in a foam-core box. We also allow all electronics associated with the microscope to warm up for a few hours before starting an experiment, so that any thermal gradients can equilibrate.

The coverslip and flow cells are mounted on a motorized three-axis stage (MAX343, Thorlabs) that has stepper motors for coarse adjustments and piezoelectric actuators for fine adjustments. The fine adjustments are used for active stabilization, as discussed below.

Active stabilization

The position of the coverslip relative to the objective is actively stabilized in all three dimensions. Each dimension is controlled separately through a proportional control loop on the PC. During each iteration of the loop, the position of the coverslip is measured, and the

bioRxiv preprint doi: https://doi.org/10.1101/265330; this version posted February 14, 2018. The copyright holder for this preprint (which was not certified by peer review) is the author/funder. All rights reserved. No reuse allowed without permission.

voltage driving the piezoelectric actuators is modified to keep the coverslip in its original position. The active stabilization maintains the position of the coverslip to within a few nanometers in each dimension (Supplementary Figure **3**).

The height of the coverslip above the objective is measured by tracking the position of a laser (red in Figure **1**a) that is totally internally reflected by the coverslip-water interface, as described by Ortega-Arroyo and coworkers.[31] We use a 785-nm, 90 mW, single-mode diode laser (L785P090, Thorlabs) that is coupled through a single-mode fiber (fiber 2; S630-HP, Thorlabs). The laser is driven with a constant current (27 mA) that is well below threshold (35 mA), which we find improves the intensity stability of the laser. After exiting the optical fiber, the beam is collected by lens 2 (plano-convex, focal length = 20 mm, Thorlabs), reflects from a dichroic mirror (700 nm short-pass, Edmund Optics), and is focused onto the back aperture of the objective. We align the beam so that after exiting the objective, it totally internally reflects from the coverslip-water interface and re-enters the objective. The total power incident on the coverslip is less than 1 μW. The return beam reflects from the coverslip and then from a D-shaped mirror (Thorlabs) and is detected with camera 2 (DCC1545M, Thorlabs). A long-pass filter (700-nm, Thorlabs, not shown in Figure **1**a) attenuates any light from the imaging beam that is also incident on camera 2. We measure the position of the return beam by determining the center-of-brightness of the image recorded by camera 2. When the height of the coverslip changes, the return beam is displaced laterally across camera 2, resulting in a change in the measured center-of-brightness. Under active stabilization, any changes in the center-of-brightness are measured and corrected every 30 ms.

The in-plane position of the coverslip is measured by tracking a 30-nm gold particle that is adsorbed to the coverslip surface (see next subsection for details of how we prepare the coverslips). Before each experiment, we find one of the adsorbed gold particles by looking for spots that have a normalized intensity of approximately 0.2. We then move the coverslip so that the spot is near the edge of the field of view. Using a 16 × 16-pixel region of the field of view, we record a static background image of the coverslip with no particles present and

bioRxiv preprint doi: https://doi.org/10.1101/265330; this version posted February 14, 2018. The copyright holder for this preprint (which was not certified by peer review) is the author/funder. All rights reserved. No reuse allowed without permission.

then move the gold particle into the center of this small field of view. Before tracking the position of the gold particle, we process its image in the small field of view by subtracting off the static background, applying a bandpass filter (passing features of size 1 to 7 pixels) to smooth the image, and taking the time-median of 33 images of the particle (recorded at 33 Hz) to reduce shot noise. We then use the program Trackpy[54] to locate the center of the particle. We use this position for the active stabilization loop, which runs once per second. The in-plane control loop frequency (1 Hz) is lower than that of the out-of-plane control loop (33 Hz) because of the time required to collect the median image of the particle.

Coverslip and gold nanoparticle functionalization

We find that many brands of #2 coverslips are unsuitable for assembly measurements because they have imperfections that scatter too much light. We use only #2 thickness, 24 mm × 60 mm rectangular glass microscope coverslips from Globe Scientific, Inc.

We adapt the protocols described by Joo and Ha[55] to coat the coverslips with a layer of PEG molecules, about 1% of which are functionalized with short DNA oligonucleotides. Briefly, we treat the coverslips with (3-aminopropyl)triethoxysilane (APTES) (99%, Sigma-Aldrich) to impart a positive surface charge when the coverslips are submerged in neutral-pH buffer. The coverslips can then nonspecifically bind oppositely charged macroions such as nucleic acids and MS2 capsids (Figure **3**). Furthermore, the layer of amino groups can form covalent linkages through *N*-hydroxysuccinimide (NHS) chemistry. We form the PEG layer by adding 90-μL of 100 mM sodium bicarbonate buffer containing 9 mg of a 100:1 mixture of 5,000-Da NHS-PEG (> 95%, Nanocs) and 5,000-Da NHS-PEG-N_3 (purity unreported, Nanocs) between two APTES-functionalized coverslips and then letting the "sandwich" sit overnight at room temperature in a humid box before washing the slips with deionized water (obtained from a Millipore RNase-free system; Synthesis, Milli-Q). We attach DNA oligonucleotides to the surface-bound NHS-PEG-N_3 molecules by copper-free click chemistry. The 20-base-long oligonucleotides are synthesized with a dibenzocyclooctyne (DBCO) group

bioRxiv preprint doi: https://doi.org/10.1101/265330; this version posted February 14, 2018. The copyright holder for this preprint (which was not certified by peer review) is the author/funder. All rights reserved. No reuse allowed without permission.

on the 5'-end (RNase-free HPLC purified, Integrated DNA Technologies). We place 90 μL of 10 μM DBCO-DNA in phosphate-buffered saline (PBS without Ca or Mg, Lonza) between two coverslips and let the sandwich sit overnight at room temperature in a humid box. The sequence of the surface oligo is `5'-(DBCO)-GGTTGGTTGGTTGGTTGGTT-3'`

We decorate the functionalized coverslips with 30-nm gold particles that serve as tracer particles for active stabilization. We purchase 30-nm amine-functionalized particles (Nanopartz) and conjugate them to NHS-PEG to prevent adsorption of coat proteins. The conjugation is done by adding 20 mg of NHS-PEG to 200 μL of 10 nM of gold particles in 100 mM sodium bicarbonate buffer. The mixture is left overnight in a tube rotator. The particles are then washed five times by centrifuging the mixture at 8,000 g for 5 min and then resuspending in TE buffer (10 mM tris-HCl, pH 7.5; 1 mM EDTA). To allow the the PEG-passivated gold particles to bind non-specifically to the coverslip, we sandwich 70 μL of 0.1 nM suspension of the particles between two coverslips and let them sit for 10 min at room temperature before washing the slips with deionized water. The method produces an average surface density of about 1 particle per 100 μm^2, as measured in the interferometric scattering microscope. Functionalized coverslips are stored under nitrogen gas at −20 °C and discarded after 2 months.

Flow cell design and construction

We build chips that each contain 10 separate flow cells above a single coverslip. Each chip consists of two sheets of cut, clear acrylic that are sealed together and to the coverslip with melted Parafilm (Bemis), as described in the following paragraphs. A cross section of a flow cell is shown in Figure 1b. Each flow cell has an imaging chamber that is used for the assembly experiments, an inlet cup to hold fluid before it is introduced into the imaging chamber of the flow cell, a short inlet chamber to connect the inlet cup to the imaging chamber, and an outlet chamber.

A schematic of each of the layers of the chip is shown in Supplementary Figure 4. The

bioRxiv preprint doi: https://doi.org/10.1101/265330; this version posted February 14, 2018. The copyright holder for this preprint (which was not certified by peer review) is the author/funder. All rights reserved. No reuse allowed without permission.

bottom acrylic sheet (Optix Acrylic, ePlastics) is 0.75 mm thick and contains 10 rectangular through-holes (1 mm × and 4.6 mm) that are cut with a laser cutter (HSE 150W, KERN). These rectangular holes form the imaging chamber of each flow cell. The top acrylic sheet (6.35 mm thick cast acrylic, McMaster-Carr) serves as the roof of the imaging chambers and contains the inlet cups, the inlet chambers, and the outlet chambers. Each inlet cup is 3.35 mm deep and 4 mm in diameter. Each inlet chamber is a 1-mm-diameter through-hole that begins at the base of an inlet cup and connects to an imaging chamber in the bottom acrylic sheet. The outlet chambers are 1.6 mm-diameter through-holes. We epoxy (5 minute epoxy, Devcon) a 10-mm-long aluminum tube (inner diameter 0.9 mm, outer diameter 1.6 mm, McMaster-Carr) into each outlet chamber. All holes in the top acrylic piece are machined with a mill. The Parafilm sheets used to seal together the layers of the flow cell contain rectangular gaps that are the same size as the imaging chambers. The gaps are cut with a computer-controlled vinyl cutter (CAMM-1 Servo, Roland).

To assemble each chip, we first clean the acrylic sheets and Parafilm by sonicating in a 2% w/v aqueous solution of sodium dodecyl sulfate (> 99%, Sigma-Aldrich) for 30 min. After sonicating, we rinse the acrylic and Parafilm with deionized water and then dry them under a stream of nitrogen gas. Next, we press one sheet of Parafilm onto the bottom acrylic sheet so that the Parafilm and acrylic stick together, and we place this assembly in a 65 °C oven for 5 min. The top acrylic sheet is also placed in the oven for 5 min. When we remove the acrylic sheets from the oven and press them firmly together, the melted Parafilm seals the two sheets of acrylic together to form the chip. We then press the other sheet of Parafilm onto the bottom of the chip so that it sticks, and we place the chip in a 65 °C oven for 5 min. We remove the chip from the oven and press it firmly onto the functionalized coverslip (which is not heated) to seal the chip to the coverslip. We use all of the flow cells on a coverslip within one or two days.

We inject buffer solution into each imaging chamber using a plastic syringe (3 mL BD, VWR) that is connected to the aluminum outlet tube by a short (approximately 4 cm) length

bioRxiv preprint doi: https://doi.org/10.1101/265330; this version posted February 14, 2018. The copyright holder for this preprint (which was not certified by peer review) is the author/funder. All rights reserved. No reuse allowed without permission.

of tubing (Tygon PVC, McMaster-Carr). We fill the inlet cup with solution and then pull it through the imaging chamber by actuating the syringe with a motorized linear translation stage (PT1-Z8, Thorlabs). Each time we inject a solution into the imaging chamber, we use the motorized stage to inject 10 μL of solution at a constant rate over 20 s. Before further injections we use a Kimwipe (Kimberly-Clark Professional) to wick any remaining solution from the inlet cup. To ensure that the fluid injection is reproducible, we prevent any air bubbles from entering the flow cell, tubing, or syringe. We mount the syringe vertically to prevent air bubbles from being trapped inside it.

We recommend against using soft materials (such as polydimethylsiloxane) to build the flow cells. We find that soft materials lead to more warping of the coverslip during injection. We also find that higher flow velocities and chambers with smaller cross-sections increase warping, owing to the higher pressures.

Growth of MS2 and purification of its coat protein and RNA

We grow *wild-type* MS2 by infecting liquid cultures of *E. coli* strain C3000 (a gift from Peter Stockley at the University of Leeds) and purifying the progeny virions following the protocols of Strauss and Sinsheimer.[56] The final concentration of MS2 is determined by UV-spectrophotometry (NanoDrop 1000, Thermo Scientific) (Supplementary Figure **1**), assuming an extinction coefficient of 8.03 mL mg^{-1} cm^{-1} at 260 nm.[56] We store the purified virus particles at 4 °C and discard them after 1 month.

We purify coat protein from the virus particles following the cold acetic acid method described by Sugiyama, Hebert, and Hartmann.[4] Then we exchange the coat protein buffer for 20 mM acetic acid using 3-kDa-MWCO centrifugal filter units (EMD Millipore). In 20 mM acetic acid, the coat proteins form non-covalent dimers. We determine the concentration of coat-protein dimers by UV-spectrophotometry (Supplementary Figure **1**), using an extinction coefficient of 33200 M^{-1} cm^{-1} at 280 nm.[11] We check for RNA contamination by measuring the ratio of the UV-absorbance at 260 nm to that at 280 nm. We use only

bioRxiv preprint doi: https://doi.org/10.1101/265330; this version posted February 14, 2018. The copyright holder for this preprint (which was not certified by peer review) is the author/funder. All rights reserved. No reuse allowed without permission.

protein that has a 260/280 ratio less than 0.67 for assembly. We store the protein at 4 °C and discard it after 1 week.

We purify RNA from freshly grown MS2 virions using an RNA extraction kit (RNeasy, Qiagen). We collect the RNA in TE buffer (10 mM Tris-HCl, pH 7.5; 1 mM EDTA) and determine its concentration using an extinction coefficient of 0.025 mL mg^{-1} cm^{-1} at 260 nm. We check for protein contamination by measuring the ratio of the UV-absorbance at 260 nm to that at 280 nm (Supplementary Figure 1). We use only RNA that has a 260/280 ratio greater than 2.0 for assembly. Then we check the integrity of the RNA by native 1% agarose gel electrophoresis (Supplementary Figure 2). We store the RNA at −80 °C and discard it after 1 year.

Surface-immobilization of MS2 RNA by DNA linkages

To immobilize MS2 RNA at the coverslip surface, we first hybridize the 5'-end of the RNA to a 60-base-long linker oligo (Integrated DNA Technologies). The 40 bases at the 5'-end of the linker are complementary to the 40 bases at the 5'-end of the RNA, and the remaining 20 bases are complementary to the sequence of the surface oligo. To anneal the linker to the MS2 RNA, we add a 10-fold molar excess of the linker oligo to 500 nM of MS2 RNA in hybridization buffer (50 mM Tris-HCl, pH 7.0; 200 mM NaCl, 1 mM EDTA), heat the mixture to 90 °C for 1 s, and then cool it to 4 °C at a rate of −1 °C/s. Excess linker is removed with a 100-kDa-MWCO centrifugal filter unit (EMD Millipore) at 14,000 g. At this centrifugal force, the 60-base-long oligonucleotides do not pass through the filter; instead, they stick to the membrane. We confirm RNA-DNA binding by native 1% agarose gel electrophoresis (Supplementary Figure 2) and interferometric scattering microscopy (Supplementary Figure 6). The sequence of the linker is `5'-CGACAGGAAGTTGAGCAGGACCCCGAAAGGGGTCCCACCCAACCAACCAACCAACCAACC-3'`

bioRxiv preprint doi: https://doi.org/10.1101/265330; this version posted February 14, 2018. The copyright holder for this preprint (which was not certified by peer review) is the author/funder. All rights reserved. No reuse allowed without permission.

Calibration experiment protocol

We measure the intensities of MS2 RNA and *wild-type* MS2 virus particles (Figure **3**) by imaging the particles as they adsorb to an APTES-functionalized coverslip. For these experiments we do not use a flow cell. Instead, we use a "lean-to" sample chamber made of 1-mm-thick glass slides (Micro Slides, Corning) that are cut, cleaned by pyrolysis (PYRO-CLEAN, Tempyrox Co.), and sealed in place with vacuum grease (High vacuum grease, Dow Corning). This sample chamber is described in detail in a previous paper.[30] To perform the calibration experiment, we first fill the sample chamber with TNE buffer (50 mM Tris-HCl, pH 7.5; 100 mM NaCl; 1 mM EDTA) and focus the microscope onto the coverslip. We then exchange the buffer in the sample chamber with a solution containing both MS2 RNA and *wild-type* MS2 virus particles at a concentration of 0.1 nM each in TNE buffer. We record movies (100 Hz) of these particles nonspecifically adsorbing to the coverslip.

We see two well-separated peaks in the histogram of the intensities of the particles after they bind (Figure **3**). We assume that the lower-intensity peak is due to the RNA molecules and the higher-intensity peak is due to the MS2 viruses. To determine the median and width of each intensity peak, we separate the two using an intensity threshold (0.003) that lies between them.

Assembly experiment protocol

For assembly experiments, we fill a flow cell with hybridization buffer containing 0.2% Tween-20 (Sigma-Aldrich) and let it sit for 10 min. We find that this 10-min incubation with Tween-20 prevents the MS2 coat protein from adsorbing to the coverslip through defects in the PEG layer. Next, we flush out the Tween-20 with fresh hybridization buffer, find the center of the imaging chamber, focus the microscope onto the coverslip, and begin the out-of-plane active stabilization control loop. Then we locate a 30-nm gold particle within 50 μm of the center of the imaging chamber and start the in-plane active stabilization control loop. With the setup actively stabilized in all three dimensions, we inject 1 nM of RNA-DNA complexes

bioRxiv preprint doi: https://doi.org/10.1101/265330; this version posted February 14, 2018. The copyright holder for this preprint (which was not certified by peer review) is the author/funder. All rights reserved. No reuse allowed without permission.

in hybridization buffer and record a short movie of them adsorbing to the coverslip. After 10–100 complexes bind, we flush the imaging chamber by pumping 120 μL of assembly buffer through the chamber over the course of 12 min. Then we start recording a movie and inject 2 μM of coat-protein dimers in assembly buffer. The injection starts 4 s into the movie.

Image processing of the interferometric scattering microscope images

Image processing is required to normalize the raw images and to reduce fluctuations in the background intensity. We apply an approach similar to the "pseudo-flat-fielding" method described by Ortega-Arroyo and coworkers.[31] The images in Figures **1**, **3**, and **4** are processed in this way, as are all the movies included in the Supplementary Information.

Each raw image, denoted I_{raw}, is processed according to the following steps: First, a dark image, I_{dark}, is acquired by taking the time-median of many frames (200 frames for 100 Hz data and 2,000 for 1,000 Hz data) when the illumination beam is blocked. This image is subtracted from each raw image, yielding $I_{\mathrm{bkgd}} = I_{\mathrm{raw}} - I_{\mathrm{dark}}$. Second, features bigger than $\sigma_1 = 1.5$ pixels are removed by subtracting a Gaussian blur, yielding $I_{\mathrm{smooth}} = I_{\mathrm{bkgd}} - \mathrm{blur}(I_{\mathrm{bkgd}}, \sigma_1)$, where $\mathrm{blur}(I, \sigma)$ is 2D Gaussian blur of the image, I, using a standard deviation σ. We choose $\sigma_1 = 1.5$ to minimize intensity changes that arise from time-varying background fringes, even though this choice slightly decreases the normalized intensities of the particles and assemblies on the coverslip. Third, the image is normalized to the background that has been blurred with $\sigma_2 = 20$ pixels, so that particles on the coverslip and stray fringes smaller than σ_2 do not affect the normalization. This process yields $I_{\mathrm{norm}} = (I_{\mathrm{smooth}})/\mathrm{blur}(I_{\mathrm{bkgd}}, \sigma_2)$. Because each image is normalized independently of other images in the time-series, fluctuations in the illumination intensity in time do not affect I_{norm}. Finally, all remaining static features in the background are removed by subtracting the time-median of many frames (300 frames for 100 Hz data and 3,000 for 1,000 Hz data) of the movie, yielding the final processed image $I_{\mathrm{final}} = I_{\mathrm{norm}} - I_{\mathrm{norm,med}}$. The noise in I_{final} is set by shot noise for the first few seconds after the background subtraction, but after this time,

bioRxiv preprint doi: https://doi.org/10.1101/265330; this version posted February 14, 2018. The copyright holder for this preprint (which was not certified by peer review) is the author/funder. All rights reserved. No reuse allowed without permission.

fluctuations in the background intensity due to uncorrected mechanical drift are the main source of measurement noise.

We extract the intensity as a function of time for particles adsorbing to the coverslip and for protein assemblies from the processed movies in the following way: First, we manually locate the center position of the image of each particle or assembly. Then we measure the mean intensity in a circle of radius 1 pixel that is centered on the particle or assembly. The intensities displayed in Figure **3** are determined by measuring the changes in intensity when the RNA or *wild-type* virus particle adsorbs to the coverslip.

Because particles as faint as MS2 virions and the MS2 RNA cannot be seen in the raw images, we perform a simplified, real-time image processing routine to see such faint particles while collecting data. The routine consists of a simple background division and a moving time-average. It is implemented with a Python script that enables us to view images and control the camera (http://github.com/manoharan-lab/camera-controller). The active stabilization feedback loops are also implemented in the same script.

TEM of assemblies

We use TEM and negative staining to image the protein assemblies that form on MS2 RNA that is tethered to the surface of 30-nm gold particles (Figure **2**b, Supplementary Figure **5**). The surfaces of the gold particles are functionalized in a way that is similar to that used for the coverslips. The protocol is identical to that used to prepare the tracer particles for active stabilization, except that we use NHS-PEG-N_3 instead of NHS-PEG. To conjugate DNA oligonucleotides to the PEG-coated gold particles, we add 5 μM of DBCO-DNA to 10 nM of gold particles in PBS without Ca or Mg. The mixture is left at room temperature overnight in a tube rotator and then washed 5 times by centrifuging the mixture at 8,000 g for 5 min and resuspending in TE buffer.

To perform the assembly reaction, we add a 100-fold molar excess of RNA-DNA complexes (20 nM) to the gold particles (0.2 nM) and equilibrate the mixture in TNE buffer for

bioRxiv preprint doi: https://doi.org/10.1101/265330; this version posted February 14, 2018. The copyright holder for this preprint (which was not certified by peer review) is the author/funder. All rights reserved. No reuse allowed without permission.

1 hr on ice. We then take 6 μL of this mixture, add 0.42 μL of 30 μM of coat-protein dimers suspended in 20 mM acetic acid, and let the mixture sit for 10 min at room temperature. The mixture is then added to a plasma-etched carbon-coated TEM gird (Ted Pella), left to sit for 1 min, and then removed by blotting with filter paper. Then 6 μL of methylamine tungstate stain solution (Nanoprobes) is added and left to sit for 1 min before removal by blotting with filter paper. We visualize the samples on a Tecnai F20 (FEI) transmission electron microscope operated at 120 kV. Images are captured on a 4,096 × 4,096-pixel CCD camera (Gatan). Representative images are shown in Supplementary Figure 5 along with images of control reactions involving bare RNA without the DNA linkage.

Acknowledgement

We thank Peter Stockley and Amy Barker at the University of Leeds for sending us initial stocks of MS2 virus and C3000 cells. We thank Philip Kukura, Marek Piliarik, Vahid Sandoghdar, and Michael Brenner for helpful discussions. This work is supported by the Harvard MRSEC under National Science Foundation grant no. DMR-1420570. Additionally, this material is based upon work supported in part by the National Science Foundation Graduate Research Fellowship under Award No. DGE-1144152. It was performed in part at the Center for Nanoscale Systems (CNS), a member of the National Nanotechnology Coordinated Infrastructure Network (NNCI), which is supported by the National Science Foundation under NSF award no. 1541959. CNS is part of Harvard University.

Author contribution

V.N.M. came up with the idea of studying virus self-assembly using interferometric scattering microscopy and developed this idea with R.F.G. and A.M.G. A.M.G. and R.F.G. designed the experimental setup, performed the experiments, and analyzed the data. V.N.M. supervised the project. A.M.G., R.F.G., and V.N.M. wrote the manuscript.

bioRxiv preprint doi: https://doi.org/10.1101/265330; this version posted February 14, 2018. The copyright holder for this preprint (which was not certified by peer review) is the author/funder. All rights reserved. No reuse allowed without permission.

References

(1) Whitesides, G.; Mathias, J.; Seto, C. Molecular self-assembly and nanochemistry: a chemical strategy for the synthesis of nanostructures. *Science* **1991**, *254*, 1312–1319.

(2) Caspar, D. L. D.; Klug, A. Physical principles in the construction of regular viruses. *Cold Spring Harbor Symposia on Quantitative Biology* **1962**, *27*, 1–24.

(3) Bancroft, J. B.; Hiebert, E. Formation of an infectious nucleoprotein from protein and nucleic acid isolated from a small spherical virus. *Virology* **1967**, *32*, 354–356.

(4) Sugiyama, T.; Hebert, R. R.; Hartman, K. A. Ribonucleoprotein complexes formed between bacteriophage MS2 RNA and MS2 protein in vitro. *Journal of Molecular Biology* **1967**, *25*, 455–463.

(5) Hohn, T. Role of RNA in the assembly process of bacteriophage fr. *Journal of Molecular Biology* **1969**, *43*, 191–200.

(6) Elrad, O. M.; Hagan, M. F. Encapsulation of a polymer by an icosahedral virus. *Physical Biology* **2010**, *7*, 045003.

(7) Perlmutter, J. D.; Perkett, M. R.; Hagan, M. F. Pathways for virus assembly around nucleic acids. *Journal of Molecular Biology* **2014**, *426*, 3148–3165.

(8) Carrillo-Tripp, M.; Shepherd, C. M.; Borelli, I. A.; Venkataraman, S.; Lander, G.; Natarajan, P.; Johnson, J. E.; Brooks, C. L.; Reddy, V. S. VIPERdb2: an enhanced and web API enabled relational database for structural virology. *Nucleic Acids Research* **2009**, *37*, 436–442.

(9) Prevelige Jr, P. E.; Thomas, D.; King, J. Nucleation and growth phases in the polymerization of coat and scaffolding subunits into icosahedral procapsid shells. *Biophysical Journal* **1993**, *64*, 824.

bioRxiv preprint doi: https://doi.org/10.1101/265330; this version posted February 14, 2018. The copyright holder for this preprint (which was not certified by peer review) is the author/funder. All rights reserved. No reuse allowed without permission.

(10) Zlotnick, A.; Johnson, J. M.; Wingfield, P. W.; Stahl, S. J.; Endres, D. A theoretical model successfully identifies features of hepatitis B virus capsid assembly. *Biochemistry* **1999**, *38*, 14644–14652.

(11) Borodavka, A.; Tuma, R.; Stockley, P. G. Evidence that viral RNAs have evolved for efficient, two-stage packaging. *Proceedings of the National Academy of Sciences* **2012**, *109*, 15769–15774.

(12) Patel, N.; Wroblewski, E.; Leonov, G.; Phillips, S. E.; Tuma, R.; Twarock, R.; Stockley, P. G. Rewriting nature?s assembly manual for a ssRNA virus. *Proceedings of the National Academy of Sciences* **2017**, *114*, 12255–12260.

(13) Faez, S.; Lahini, Y.; Weidlich, S.; Garmann, R. F.; Wondraczek, K.; Zeisberger, M.; Schmidt, M. A.; Orrit, M.; Manoharan, V. N. Fast, label-free tracking of single viruses and weakly scattering nanoparticles in a nanofluidic optical fiber. *ACS Nano* **2015**, *9*, 12349–12357.

(14) Kondylis, P.; Zhou, J.; Harms, Z. D.; Kneller, A. R.; Lee, L. S.; Zlotnick, A.; Jacobson, S. C. Nanofluidic devices with 8 pores in series for real-time, resistive-pulse analysis of hepatitis B virus capsid assembly. *Analytical Chemistry* **2017**, *89*, 4855–4862.

(15) Kler, S.; Asor, R.; Li, C.; Ginsburg, A.; Harries, D.; Oppenheim, A.; Zlotnick, A.; Raviv, U. RNA encapsidation by SV40-derived nanoparticles follows a rapid two-state mechanism. *Journal of the American Chemical Society* **2012**, *134*, 8823–8830.

(16) Jacobsen, V.; Stoller, P.; Brunner, C.; Vogel, V.; Sandoghdar, V. Interferometric optical detection and tracking of very small gold nanoparticles at a water-glass interface. *Optics Express* **2006**, *14*, 405–414.

(17) Andrecka, J.; Spillane, K. M.; Ortega-Arroyo, J.; Kukura, P. Direct observation and control of supported lipid bilayer formation with interferometric scattering microscopy. *ACS Nano* **2013**, *7*, 10662–10670.

bioRxiv preprint doi: https://doi.org/10.1101/265330; this version posted February 14, 2018. The copyright holder for this preprint (which was not certified by peer review) is the author/funder. All rights reserved. No reuse allowed without permission.

(18) Andrecka, J.; Ortega-Arroyo, J.; Lewis, K.; Cross, R.; Kukura, P. Label-free imaging of microtubules with sub-nm precision using interferometric scattering microscopy. *Biophysical Journal* **2016**, *110*, 214–217.

(19) van Duin, J. *The Bacteriophages*; Springer, 1988; pp 117–167.

(20) Valegård, K.; Murray, J. B.; Stockley, P. G.; Stonehouse, N. J.; Liljas, L. Crystal structure of an RNA bacteriophage coat protein-operator complex. *Nature* **1994**, *371*, 623–626.

(21) Dai, X.; Li, Z.; Lai, M.; Shu, S.; Du, Y.; Zhou, Z. H.; Sun, R. In situ structures of the genome and genome-delivery apparatus in a single-stranded RNA virus. *Nature* **2017**, *541*, 112–116.

(22) Hirao, I.; Spingola, M.; Peabody, D.; Ellington, A. D. The limits of specificity: An experimental analysis with RNA aptamers to MS2 coat protein variants. *Molecular Diversity* **1998**, *4*, 75–89.

(23) Toropova, K.; Basnak, G.; Twarock, R.; Stockley, P. G.; Ranson, N. A. The three-dimensional structure of genomic RNA in bacteriophage MS2: implications for assembly. *Journal of Molecular Biology* **2008**, *375*, 824–836.

(24) Stockley, P. G.; Rolfsson, O.; Thompson, G. S.; Basnak, G.; Francese, S.; Stonehouse, N. J.; Homans, S. W.; Ashcroft, A. E. A simple, RNA-mediated allosteric switch controls the pathway to formation of a T= 3 viral capsid. *Journal of Molecular Biology* **2007**, *369*, 541–552.

(25) Rolfsson, Ó.; Middleton, S.; Manfield, I. W.; White, S. J.; Fan, B.; Vaughan, R.; Ranson, N. A.; Dykeman, E.; Twarock, R.; Ford, J.; Cheng Kao, C.; Stockley, P. G. Direct evidence for packaging signal-mediated assembly of bacteriophage MS2. *Journal of Molecular Biology* **2016**, *428*, 431–448.

bioRxiv preprint doi: https://doi.org/10.1101/265330; this version posted February 14, 2018. The copyright holder for this preprint (which was not certified by peer review) is the author/funder. All rights reserved. No reuse allowed without permission.

(26) Yusupov, M. M.; Yusupova, G. Z.; Baucom, A.; Lieberman, K.; Earnest, T. N.; Cate, J. H. D.; Noller, H. F. Crystal structure of the ribosome at 5.5 Å resolution. *Science* **2001**, *292*, 883–896.

(27) Ke, Y.; Ong, L. L.; Shih, W. M.; Yin, P. Three-dimensional structures self-assembled from DNA bricks. *Science* **2012**, *338*, 1177–1183.

(28) Park, S. Y.; Lytton-Jean, A. K. R.; Lee, B.; Weigand, S.; Schatz, G. C.; Mirkin, C. A. DNA-programmable nanoparticle crystallization. *Nature* **2008**, *451*, 553.

(29) Piliarik, M.; Sandoghdar, V. Direct optical sensing of single unlabelled proteins and super-resolution imaging of their binding sites. *Nature Communications* **2014**, *5*, 4495.

(30) Goldfain, A. M.; Garmann, R. F.; Jin, Y.; Lahini, Y.; Manoharan, V. N. Dynamic measurements of the position, orientation, and DNA content of individual unlabeled bacteriophages. *The Journal of Physical Chemistry B* **2016**, *120*, 6130–6138.

(31) Ortega-Arroyo, J.; Cole, D.; Kukura, P. Interferometric scattering microscopy and its combination with single-molecule fluorescence imaging. *Nature Protocols* **2016**, *11*, 617–633.

(32) Happel, J.; Brenner, H. *Low Reynolds number hydrodynamics*; Martinus Nijhoff Publishers, 1983.

(33) Garmann, R. F.; Sportsman, R.; Beren, C.; Manoharan, V. N.; Knobler, C. M.; Gelbart, W. M. A simple RNA-DNA scaffold templates the assembly of monofunctional virus-like particles. *Journal of the American Chemical Society* **2015**, *137*, 7584–7587.

(34) Zandi, R.; van der Schoot, P.; Reguera, D.; Kegel, W.; Reiss, H. Classical nucleation theory of virus capsids. *Biophysical Journal* **2006**, *90*, 1939–1948.

(35) Perlmutter, J. D.; Hagan, M. F. Mechanisms of virus assembly. *Annual Review of Physical Chemistry* **2015**, *66*, 217–239.

bioRxiv preprint doi: https://doi.org/10.1101/265330; this version posted February 14, 2018. The copyright holder for this preprint (which was not certified by peer review) is the author/funder. All rights reserved. No reuse allowed without permission.

(36) Wang, J. C.-Y.; Mukhopadhyay, S.; Zlotnick, A. Geometric defects and icosahedral viruses. *Viruses* **2018**, *10*.

(37) Lutomski, C. A.; Lyktey, N. A.; Zhao, Z.; Pierson, E. E.; Zlotnick, A.; Jarrold, M. F. Hepatitis B virus capsid completion occurs through error correction. *Journal of the American Chemical Society* **2017**, *139*, 16932–16938.

(38) Sorger, P. K.; Stockley, P. G.; Harrison, S. C. Structure and assembly of turnip crinkle virus: II. Mechanism of reassembly in vitro. *Journal of Molecular Biology* **1986**, *191*, 639–658.

(39) Garmann, R. F.; Comas-Garcia, M.; Gopal, A.; Knobler, C. M.; Gelbart, W. M. The assembly pathway of an icosahedral single-stranded RNA virus depends on the strength of inter-subunit attractions. *Journal of Molecular Biology* **2014**, *426*, 1050–1060.

(40) Kler, S.; Wang, J. C.-Y.; Dhason, M.; Oppenheim, A.; Zlotnick, A. Scaffold properties are a key determinant of the size and shape of self-assembled virus-derived particles. *ACS Chemical Biology* **2013**, *8*, 2753–2761.

(41) Hagan, M. F.; Elrad, O. M. Understanding the concentration dependence of viral capsid assembly kinetics—the origin of the lag time and identifying the critical nucleus size. *Biophysical Journal* **2010**, *98*, 1065–1074.

(42) Zlotnick, A.; Aldrich, R.; Johnson, J. M.; Ceres, P.; Young, M. J. Mechanism of capsid assembly for an icosahedral plant virus. *Virology* **2000**, *277*, 450–456.

(43) Chen, C.; Kao, C. C.; Dragnea, B. Self-assembly of brome mosaic virus capsids: insights from shorter time-scale experiments. *The Journal of Physical Chemistry A* **2008**, *112*, 9405–9412.

(44) Law-Hine, D.; Zeghal, M.; Bressanelli, S.; Constantin, D.; Tresset, G. Identification of

bioRxiv preprint doi: https://doi.org/10.1101/265330; this version posted February 14, 2018. The copyright holder for this preprint (which was not certified by peer review) is the author/funder. All rights reserved. No reuse allowed without permission.

a major intermediate along the self-assembly pathway of an icosahedral viral capsid by using an analytical model of a spherical patch. *Soft Matter* **2016**, *12*, 6728–6736.

(45) Medrano, M.; Fuertes, M. Á.; Valbuena, A.; Carrillo, P. J. P.; Rodrìguez-Huete, A.; Mateu, M. G. Imaging and quantitation of a succession of transient intermediates reveal the reversible self-assembly pathway of a simple icosahedral virus capsid. *Journal of the American Chemical Society* **2016**, *138*, 15385–15396.

(46) Jouvenet, N.; Simon, S. M.; Bieniasz, P. D. Visualizing HIV-1 assembly. *Journal of Molecular Biology* **2011**, *410*, 501–511.

(47) Prevelige, P. E. Follow the Yellow Brick Road: a paradigm shift in virus assembly. *Journal of Molecular Biology* **2016**, *2*, 416–418.

(48) Song, Y.; Gorbatsevych, O.; Liu, Y.; Mugavero, J.; Shen, S. H.; Ward, C. B.; Asare, E.; Jiang, P.; Paul, A. V.; Mueller, S.; Wimmer, E. Limits of variation, specific infectivity, and genome packaging of massively recoded poliovirus genomes. *Proceedings of the National Academy of Sciences* **2017**, *114*, E8731–E8740.

(49) Storhoff, J. J.; Mirkin, C. A. Programmed materials synthesis with DNA. *Chemical Reviews* **1999**, *99*, 1849–1862.

(50) Smeets, P. J.; Cho, K. R.; Kempen, R. G.; Sommerdijk, N. A.; De Yoreo, J. J. Calcium carbonate nucleation driven by ion binding in a biomimetic matrix revealed by in situ electron microscopy. *Nature Materials* **2015**, *14*, 394–399.

(51) Wang, C.; Shpaisman, H.; Hollingsworth, A. D.; Grier, D. G. Celebrating Soft Matter's 10th Anniversary: Monitoring colloidal growth with holographic microscopy. *Soft Matter* **2015**, *11*, 1062–1066.

(52) Dulin, D.; Barland, S.; Hachair, X.; Pedaci, F. Efficient illumination for microsecond tracking microscopy. *PLOS ONE* **2014**, *9*, 1–9.

bioRxiv preprint doi: https://doi.org/10.1101/265330; this version posted February 14, 2018. The copyright holder for this preprint (which was not certified by peer review) is the author/funder. All rights reserved. No reuse allowed without permission.

(53) Moerner, W.; Fromm, D. P. Methods of single-molecule fluorescence spectroscopy and microscopy. *Review of Scientific Instruments* **2003**, *74*, 3597–3619.

(54) Allan, D.; Caswell, T.; Keim, N.; van der Wel, C. Trackpy v0.3.2. 2016; https://doi.org/10.5281/zenodo.60550.

(55) Joo, C.; Ha, T. Single-Molecule FRET with total internal reflection microscopy. *Cold Spring Harbor Protocols* **2012**, 1223–1237.

(56) Strauss, J. H.; Sinsheimer, R. L. Purification and properties of bacteriophage MS2 and of its ribonucleic acid. *Journal of Molecular Biology* **1963**, *7*, 43 – 54.

(57) Foreman-Mackey, D.; Hogg, D. W.; Lang, D.; Goodman, J. emcee: The MCMC Hammer. *Publications of the Astronomical Society of the Pacific* **2013**, *125*, 306.

bioRxiv preprint doi: https://doi.org/10.1101/265330; this version posted February 14, 2018. The copyright holder for this preprint (which was not certified by peer review) is the author/funder. All rights reserved. No reuse allowed without permission.

Supplementary Information

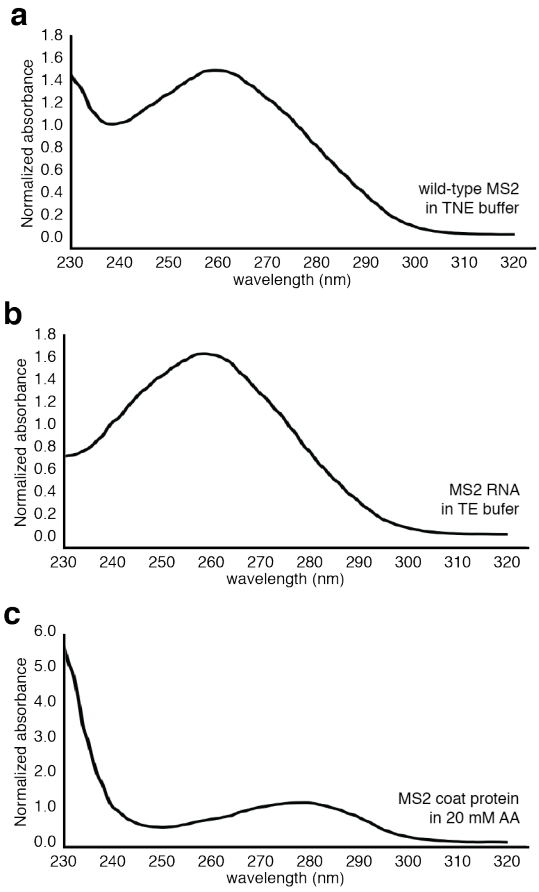

Supplementary Figure 1: **Purities of *wild-type* MS2 virus, its RNA, and its coat-protein are determined by UV-vis spectrophotometry.** Absorbance spectra for purified (a) *wild-type* MS2, (b) MS2 RNA, and (c) MS2 coat protein. The 260/280 ratio of *wild-type* MS2 in TNE buffer is 1.84, of MS2 RNA in TE buffer is 2.16, and of unassembled coat-protein dimers in 20 mM acetic acid is 0.58. Each spectrum is normalized so that the absorbance is 1.0 at 240 nm. All absorbance measurements are made using a Nanodrop-1000 spectrophotometer (Thermo Scientific).

bioRxiv preprint doi: https://doi.org/10.1101/265330; this version posted February 14, 2018. The copyright holder for this preprint (which was not certified by peer review) is the author/funder. All rights reserved. No reuse allowed without permission.

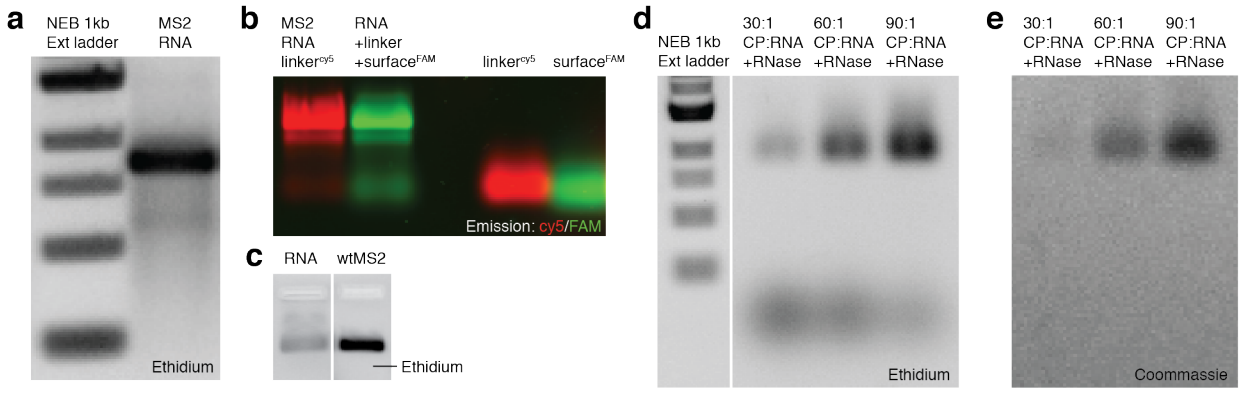

Supplementary Figure 2: **Native agarose gel electrophoresis is used to determine the integrity of the RNA, the yield of RNA-DNA hybridization, and the yield of RNA packaging by MS2 coat protein.** All gels consist of 1% agarose in TAE buffer. (a) The MS2 RNA used in the assembly experiments appears as a single band with minimal smearing, indicating that the RNA is not degraded. The left lane contains a 1-kb extended DNA ladder (New England Biolabs), and the right lane contains 1 μg of MS2 RNA. The gel is visualized after staining with Gel Red (Biotium Inc.) ethidium stain. (b) Fluorescent linker and surface oligos migrate with the RNA after hybridization and purification, indicating strong specific binding. The leftmost lane is prepared by mixing 1 μg of MS2 RNA and a 10-fold molar excess of fluorescently labeled (5'-cy5) linker oligo (Integrated DNA Technologies). The RNA is hybridized to the linker by thermal annealing, and the unbound linker is removed by centrifugal filtration. The second-to-leftmost lane is prepared by mixing 1 μg of MS2 RNA and a 10-fold molar excess of non-fluorescent linker oligo. The RNA and linker oligo are hybridized and the unbound linker purified as before. Then a stoichiometric amount of fluorescently labeled (5'-FAM) surface oligo (Integrated DNA Technologies) is added. The second-to-rightmost lane contains free 5'-cy5 linker oligo, and the rightmost contains free 5'-FAM surface oligo. The gel is visualized without staining by imaging the fluorescence emission of the cy5 and FAM dyes on separate channels. (c) MS2 RNA and *wild-type* virus particles migrate to the same position in the gel. The left lane contains RNA, and the right lane contains virus particles. The gel is visualized after staining with ethidium. (d) MS2 coat-protein dimers (CP) package MS2 RNA into RNase protected complexes with the same mobility as *wild-type* virus particles. The leftmost lane contains 1-kb extended ladder. The next three lanes are prepared by mixing 1 μg of MS2 RNA and increasing molar ratios of CP in 10 μL of TNE buffer. The mixtures are incubated for 30 min at room temperature and then treated with 10 ng of RNase A (Amresco Inc.). Electrophoresis is performed 30 min after RNase treatment, and the gel is visualized after staining with ethidium. Protected RNA migrates with the same mobility as *wild-type* virus particles, and digested RNA migrates farther down the gel. The amount of digested RNA decreases with increasing CP. (e) Assemblies prepared and then treated with RNase as just described contain protein, as evidenced by staining with coomassie (Instant Blue) protein stain.

bioRxiv preprint doi: https://doi.org/10.1101/265330; this version posted February 14, 2018. The copyright holder for this preprint (which was not certified by peer review) is the author/funder. All rights reserved. No reuse allowed without permission.

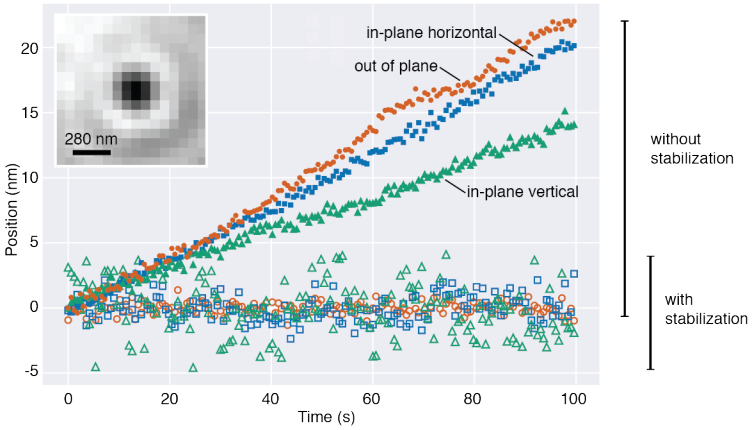

Supplementary Figure 3: **Active stabilization of the microscope.** The active stabilization routine keeps the position of the coverslip stable to within a few nanometers in all three dimensions. The plot shows the position of the stage as a function of time with active stabilization (open symbols) and without (filled symbols). The in-plane position is measured by tracking a passivated 30-nm gold nanoparticle (processed image shown in inset), and the out-of-plane position by tracking the position of a laser beam that is totally internally reflected from the coverslip-water interface.

bioRxiv preprint doi: https://doi.org/10.1101/265330; this version posted February 14, 2018. The copyright holder for this preprint (which was not certified by peer review) is the author/funder. All rights reserved. No reuse allowed without permission.

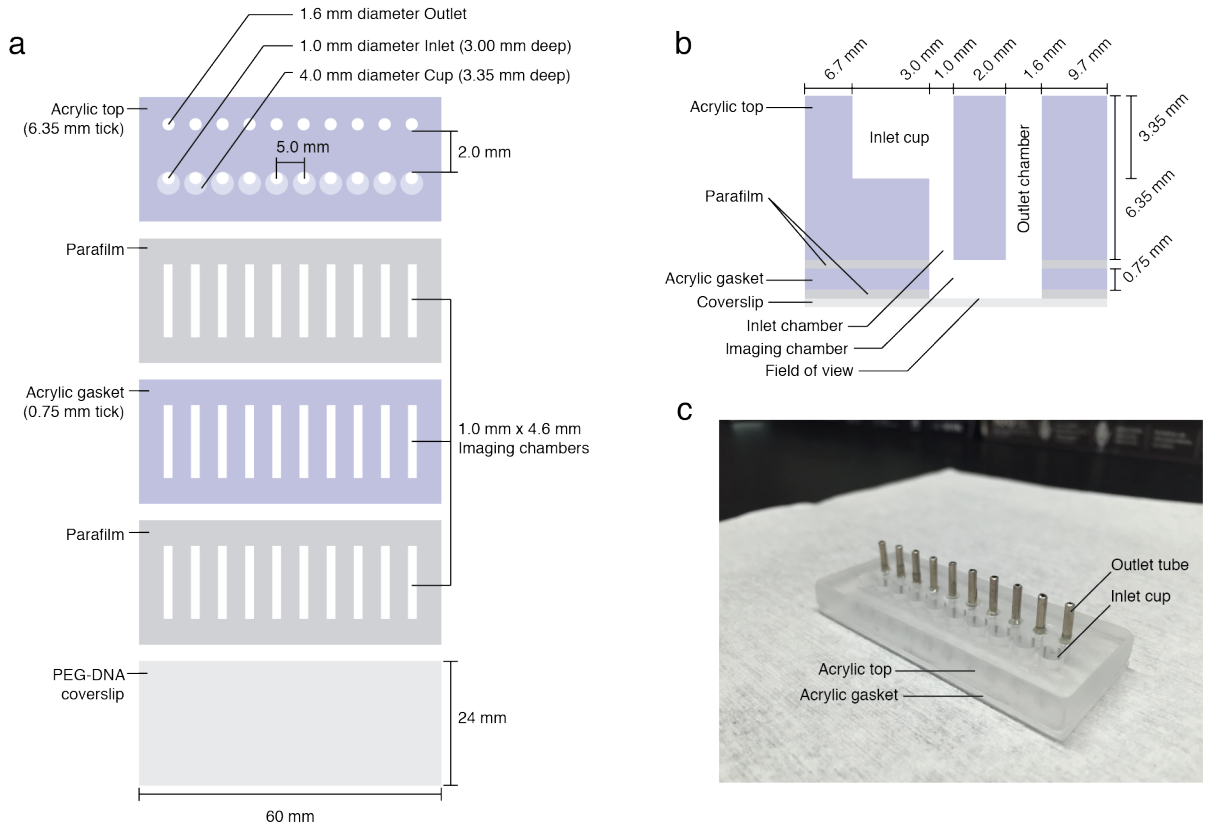

Supplementary Figure 4: **A schematic of the rigid flow cell.** (a) Each of the layers used to build the flow cell are stacked on top of one another. When heated, the parafilm seals the layers together. (b) A cross-section of a flow cell. (c) A photo of an assembled flow cell. Aluminum tubes are epoxied into the outlet chambers to connect to the Tygon tubing.

bioRxiv preprint doi: https://doi.org/10.1101/265330; this version posted February 14, 2018. The copyright holder for this preprint (which was not certified by peer review) is the author/funder. All rights reserved. No reuse allowed without permission.

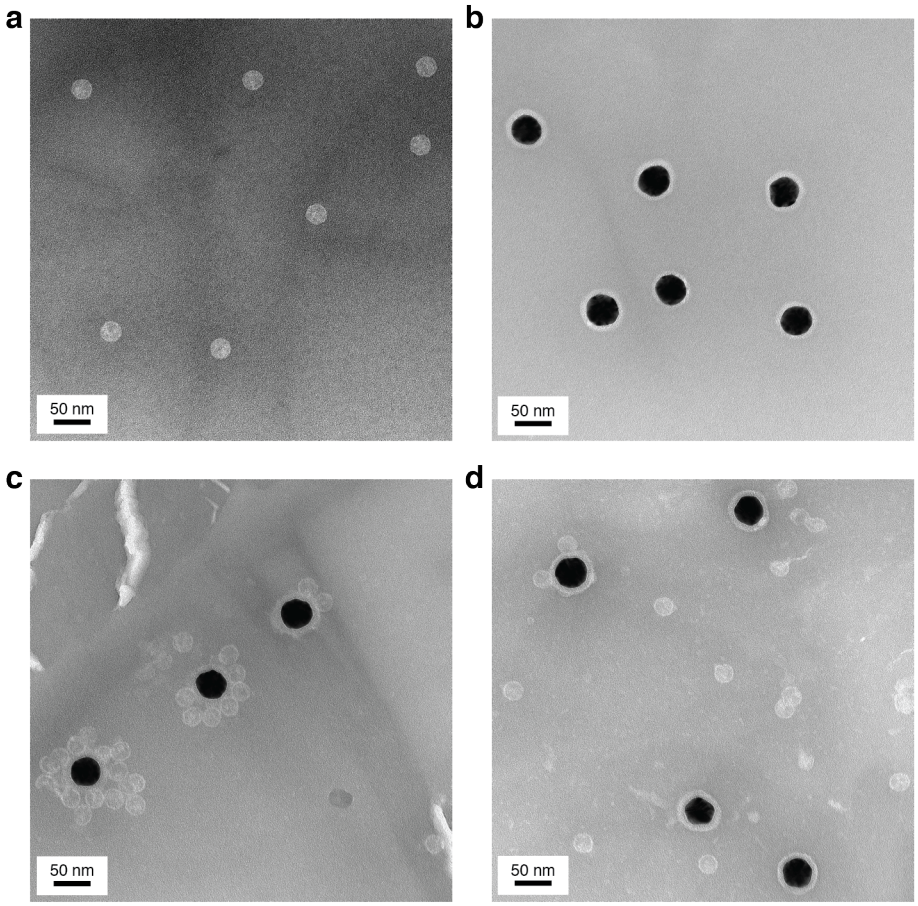

Supplementary Figure 5: Negatively stained transmission electron micrographs of virus particles, functionalized gold nanoparticles, capsids assembled around RNA molecules that are bound to the surface of the gold particles, and capsids assembled around free RNA. Each sample is stained with methylamine tungstate stain solution (Nanoprobes) before imaging. (a) *Wild-type* MS2 particles. (b) Amine-functionalized 30-nm gold nanoparticles (Nanopartz) that are coated with PEG and decorated with surface oligos. The dark spots are the gold particles, and the surrounding lighter halos are the negatively stained coatings on the particle surfaces. These coatings consist of a proprietary polymer base layer, which is applied by the manufacturer to the gold nanoparticles, and the PEG-DNA molecules that we conjugate to the particles. (c) An assembly reaction in which 2 μM of coat-protein dimers in assembly buffer is added to RNA-DNA complexes that have been incubated for 1 h with the functionalized gold particles. (d) A control reaction in which 2 μM of coat-protein dimers in assembly buffer is added to bare RNA that has been incubated for 1 h with the functionalized gold particles. The higher number of capsids near the surface of the gold particles for the experiments using RNA-DNA complexes suggests that these capsids assembled around RNA-DNA complexes that were tethered to the particle surface.

bioRxiv preprint doi: https://doi.org/10.1101/265330; this version posted February 14, 2018. The copyright holder for this preprint (which was not certified by peer review) is the author/funder. All rights reserved. No reuse allowed without permission.

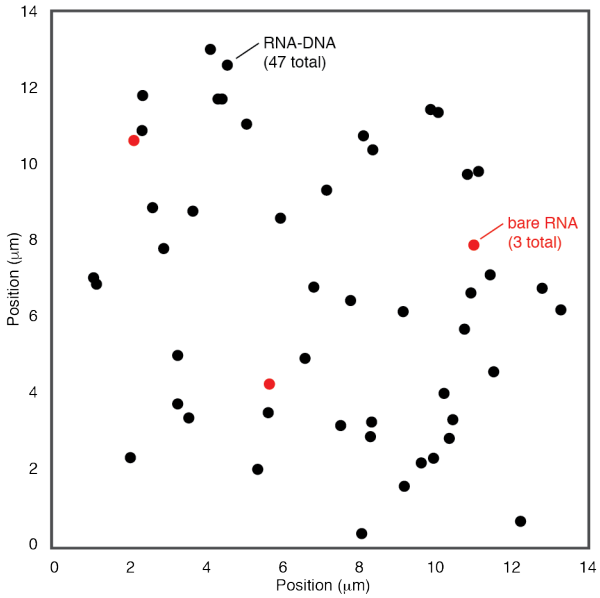

Supplementary Figure 6: **Specific binding of RNA to the coverslip via DNA linkages.** To test whether the DNA-linkage enables specific binding of the RNA to the coverslip, solutions containing 1 nM of either bare RNA or RNA-DNA complexes in hybridization buffer are injected into the imaging chamber of the interferometric scattering microscope. If the binding is specific, we expect only the RNA-DNA complexes to stick to the coverslip surface. The bare RNA is injected first, and we image the system for 60 s to detect each molecule that binds. We then inject the RNA-DNA complexes, and we repeat the measurement. The location of each detected binding event is shown: we observe a total of 3 bare RNA molecules (red circles) and 47 RNA-DNA complexes (black circles). We conclude that the binding between the RNA-DNA complexes and the coverslip is highly specific, and that most of the RNA-DNA complexes that are bound to the coverslip are tethered by a DNA linkage.

bioRxiv preprint doi: https://doi.org/10.1101/265330; this version posted February 14, 2018. The copyright holder for this preprint (which was not certified by peer review) is the author/funder. All rights reserved. No reuse allowed without permission.

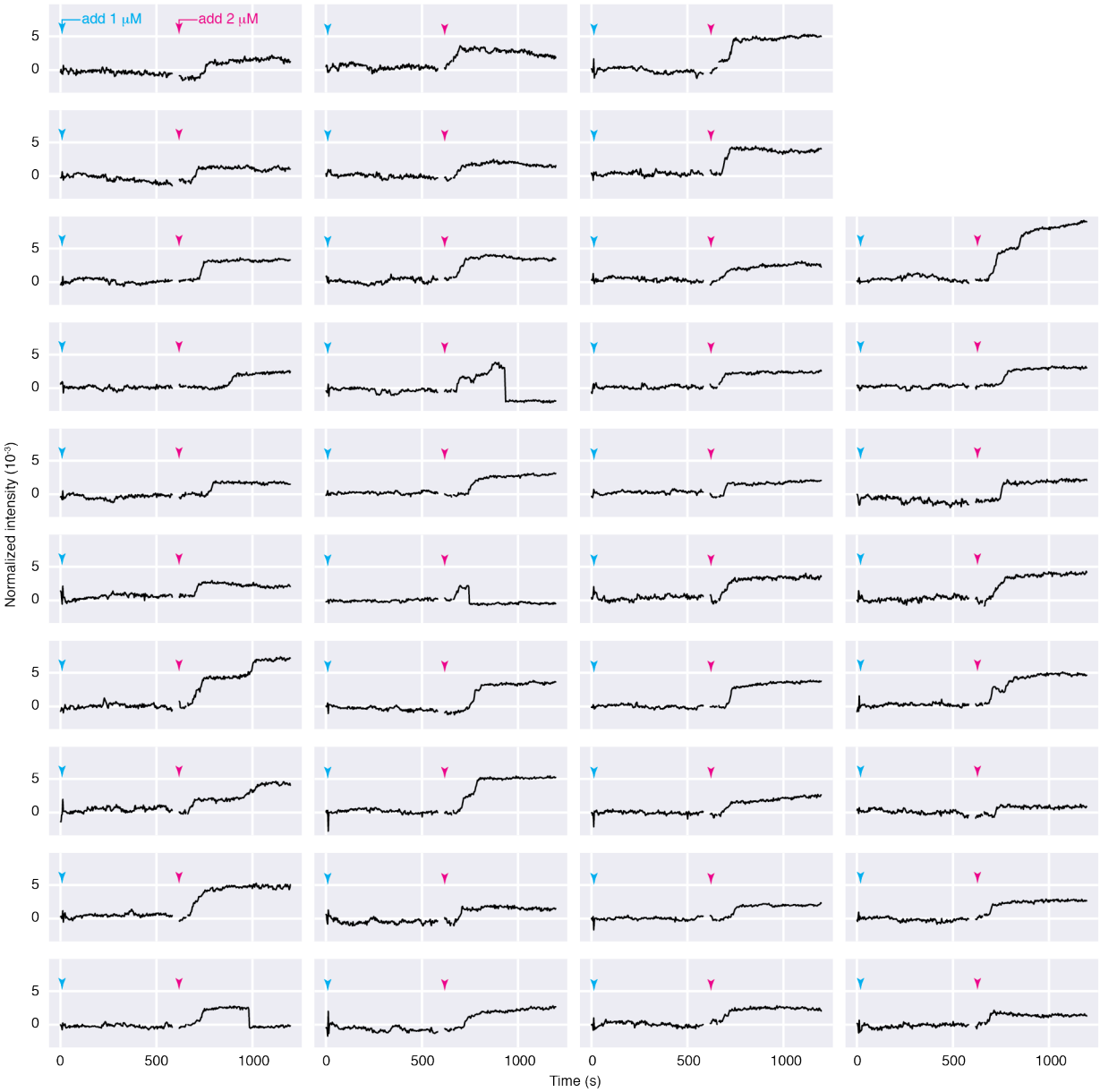

Supplementary Figure 7: **Growth curves for the 1 μM assembly discussed in the main text**. When 1 μM of coat-protein dimers is added (cyan arrowheads) to the surface-bound RNA, no assemblies appear over the course of 600 s. At this point, 2 μM of coat-protein dimers is added (pink arrowheads), after which we observe assemblies at 75 locations within the field of view. The growth curves for these assemblies are shown above. We also show the intensity plots for the first 600 s at the same locations. There is no data between 586 and 615 s, during which time we block the illumination beam and pipette in the 2 μM protein. Some curves show abrupt drops in intensity after assembly, which we interpret as detachment events, as discussed in Supplementary Figure **9**. The growth curves are measured from the data shown in Supplementary Movie 1. The data is recorded at 100 Hz and is plotted with a 300-frame average. For clarity, we show only 38 of the 75 growth curves here, and we show the remaining curves on the following page.

bioRxiv preprint doi: https://doi.org/10.1101/265330; this version posted February 14, 2018. The copyright holder for this preprint (which was not certified by peer review) is the author/funder. All rights reserved. No reuse allowed without permission.

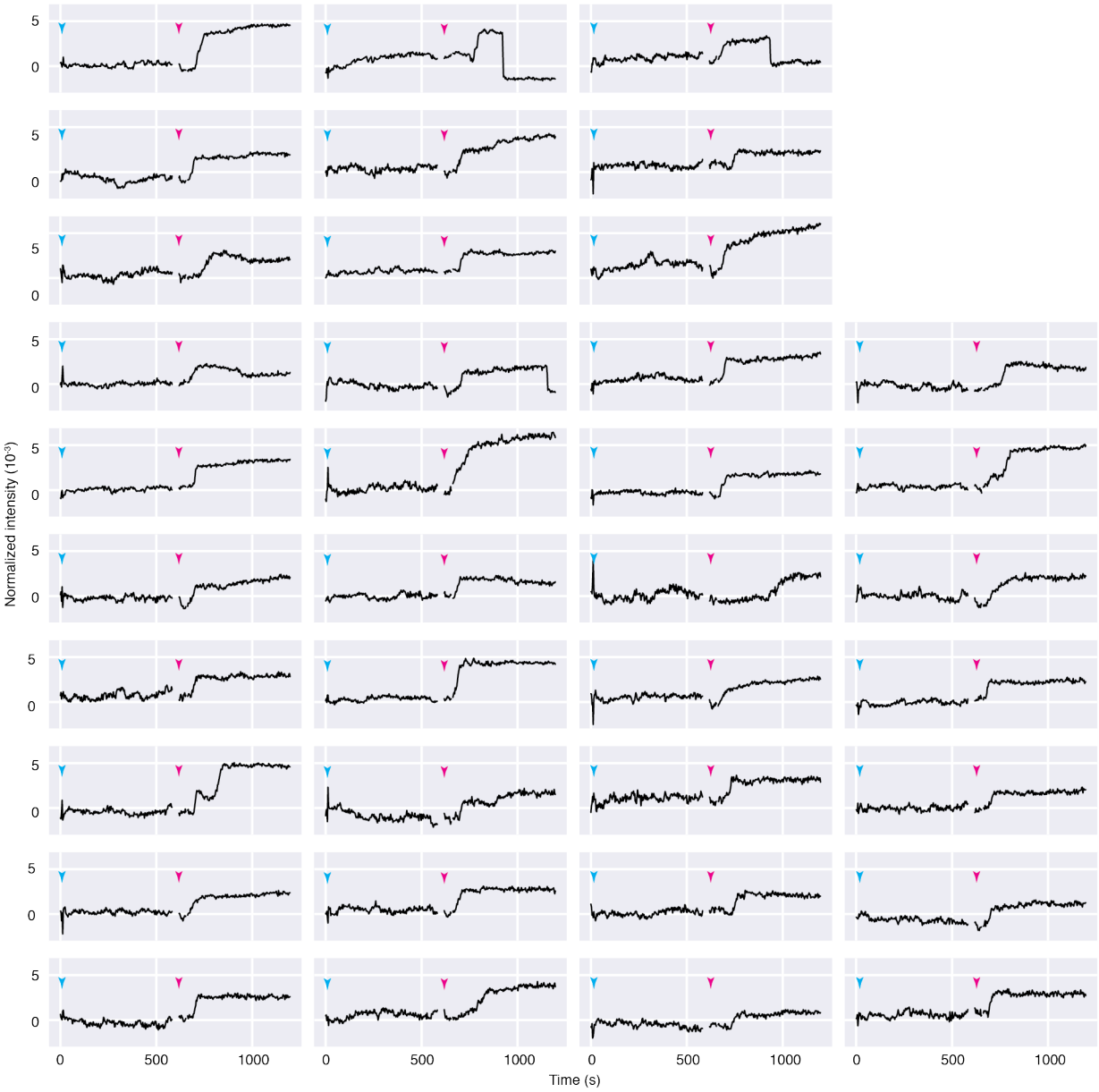

Supplementary Figure 7: **Growth curves for the 1 μM assembly discussed in the main text**. Here we show the remaining 37 growth curves described on the previous page.

bioRxiv preprint doi: https://doi.org/10.1101/265330; this version posted February 14, 2018. The copyright holder for this preprint (which was not certified by peer review) is the author/funder. All rights reserved. No reuse allowed without permission.

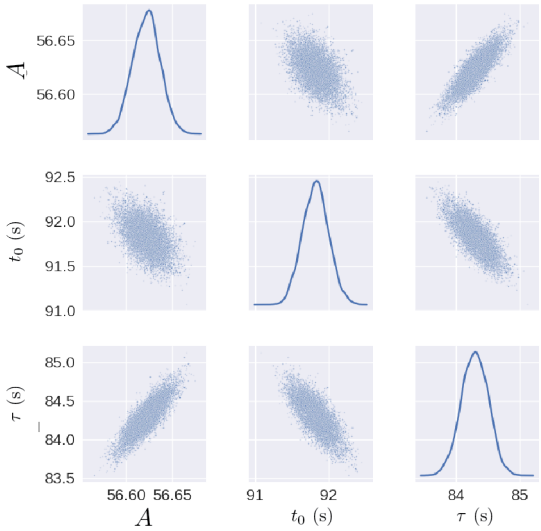

Supplementary Figure 8: **Posterior probability distributions of parameter values obtained by fitting the cumulative distribution of wait times shown in Figure 4b of the main text.** Parameters are sampled using a Markov-chain Monte Carlo technique, as discussed in the Supplementary Notes. The plots along the diagonal show kernel density estimates of the fully marginalized posterior distributions of each parameter, while the off-diagonal plots show the joint distributions.

bioRxiv preprint doi: https://doi.org/10.1101/265330; this version posted February 14, 2018. The copyright holder for this preprint (which was not certified by peer review) is the author/funder. All rights reserved. No reuse allowed without permission.

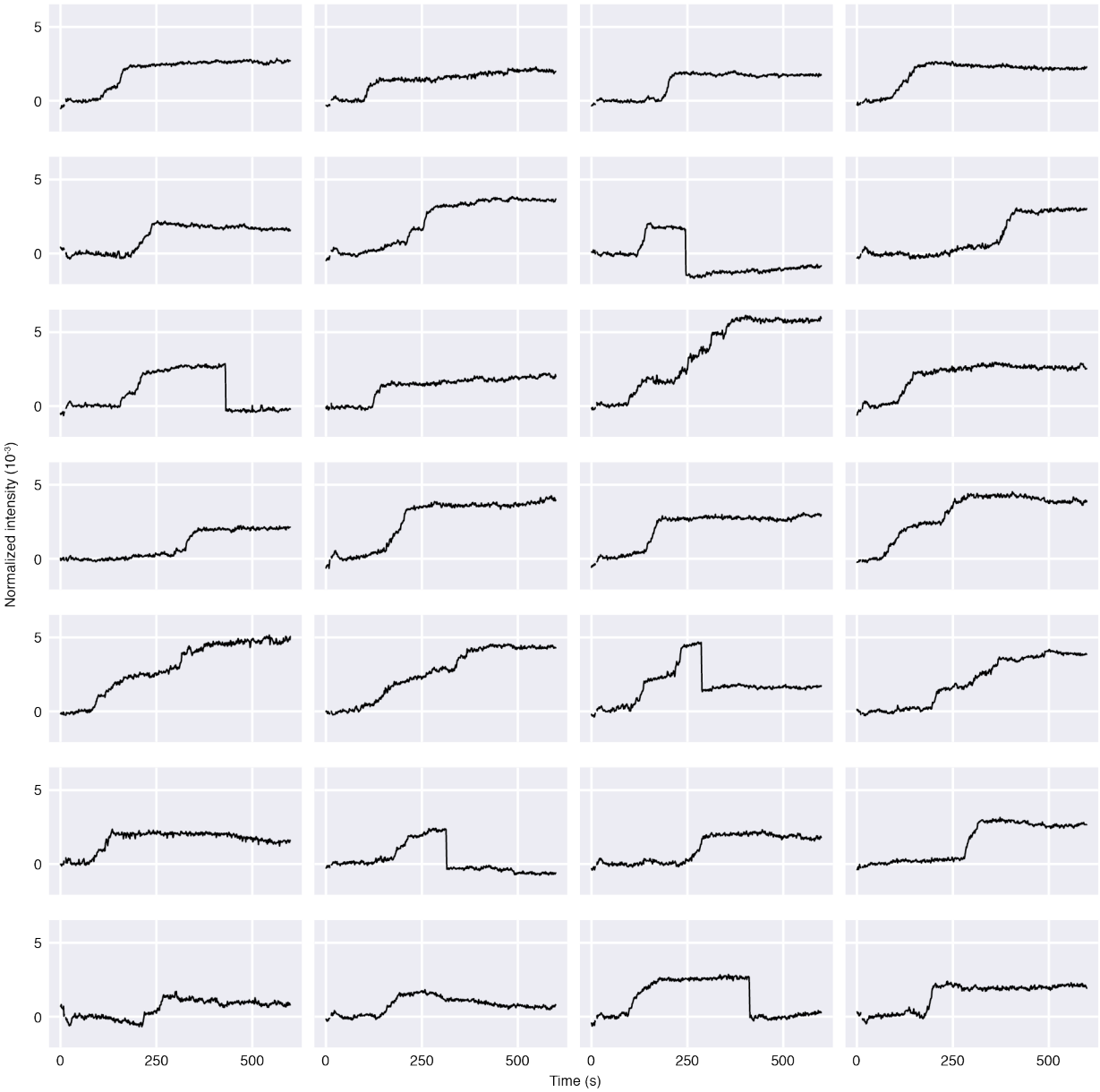

Supplementary Figure 9: **The growth curves for the assembly experiment discussed in Figure 4 of the main text.** As in Supplementary Figure 7, we interpret abrupt drops in intensity after assembly as detachment events. One of the growth curves drops to an intensity of about -0.0014, which is approximately the negative intensity of the RNA in the background image. We therefore interpret such events as the detachment of the RNA and protein assembly from the surface. Three of the growth curves drop to an intensity near 0, suggesting that the protein assembly has detached from the RNA, while the RNA remains on the surface. One of the growth curves drops from an intensity near 0.005 by an amount (0.0032) that corresponds to a full capsid, suggesting that overgrown assemblies can contain capsids. The curves are measured from the data shown in Supplementary Movie 2. The data is recorded at 1,000 Hz and is plotted with a 1,000-frame average. For clarity, we show only half of the 56 growth curves here, and the other half on the following page.

bioRxiv preprint doi: https://doi.org/10.1101/265330; this version posted February 14, 2018. The copyright holder for this preprint (which was not certified by peer review) is the author/funder. All rights reserved. No reuse allowed without permission.

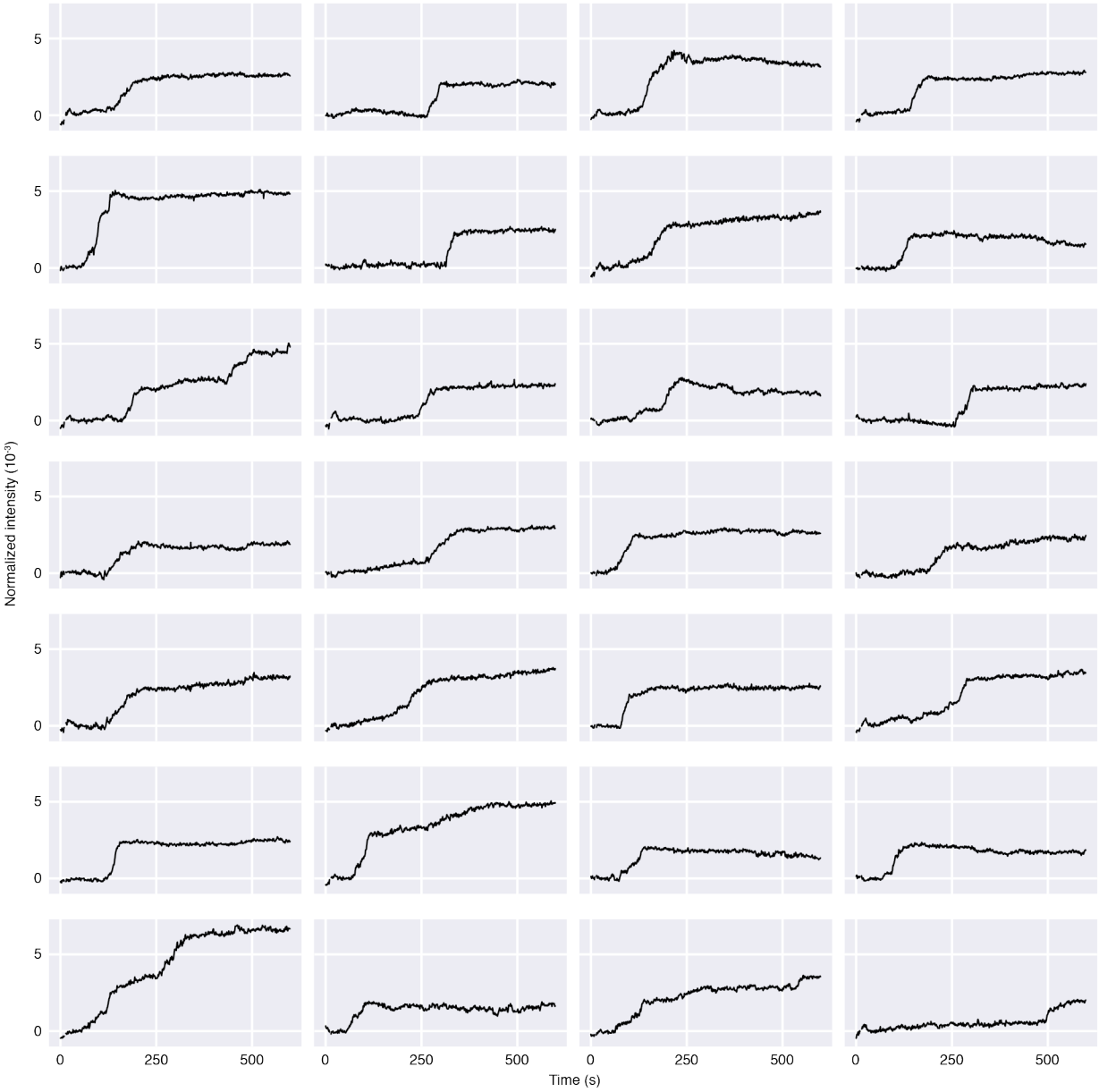

Supplementary Figure 9: The growth curves for the assembly experiment discussed in Figure 4 of the main text. Here we show the second half of the growth curves described on the previous page.

bioRxiv preprint doi: https://doi.org/10.1101/265330; this version posted February 14, 2018. The copyright holder for this preprint (which was not certified by peer review) is the author/funder. All rights reserved. No reuse allowed without permission.

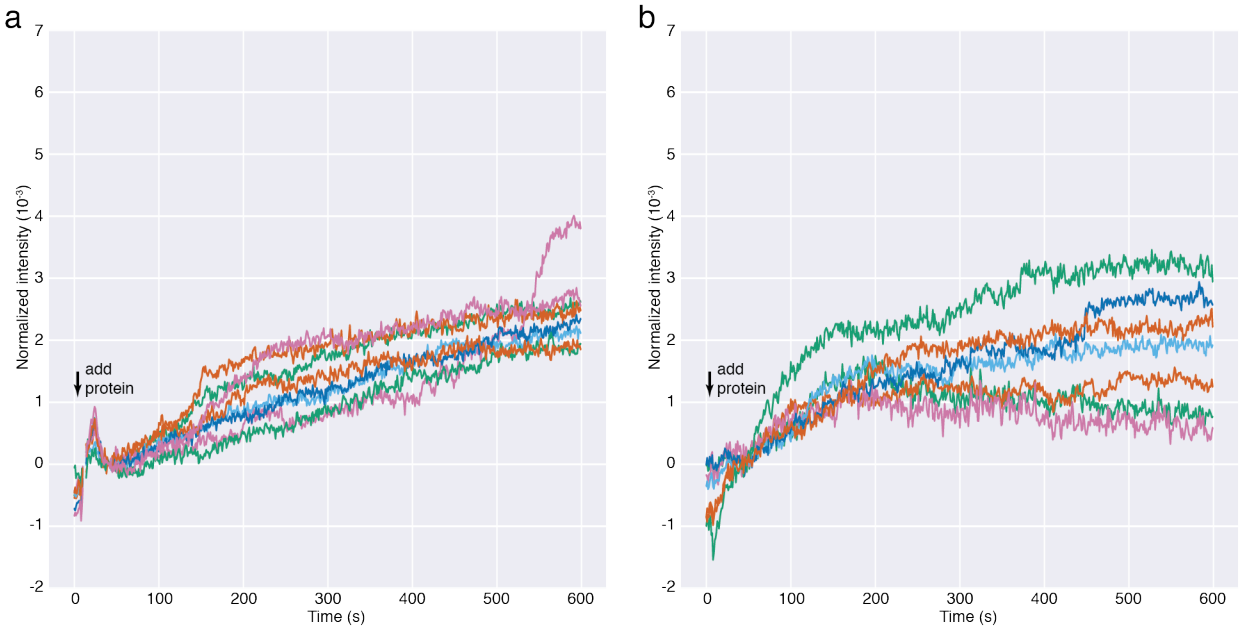

Supplementary Figure 10: **Some of the spots that appear in assembly experiments performed with 2 μM of coat-protein dimers do not represent assembly around RNA.** (a) In addition to the 56 assemblies observed in Supplementary Figure 9, we observe 8 spots that grow slowly and synchronously, and that show a consistent growth rate over the course of the measurement. Because a similar number of spots with similar growth kinetics are observed in control experiments where RNA is not added to the surface (see panel (b)), we conclude that these spots likely do *not* represent the assembly of coat-protein dimers around RNA. They may represent protein aggregates growing on the coverslip surface. As before, the curves are based on the data in Supplementary Movie 2, which is recorded at 1,000 Hz and is plotted with a 1,000-frame average. (b) In a control experiment with 2 μM of dimers but no RNA on the surface, we observe 7 spots that grow slowly and synchronously, with growth curves similar to those shown in panel (a). For this experiment, we bound the the linker oligos to the surface oligos, but we did not add the RNA. The growth curves are measured from the data in Supplementary Movie 3. The data is recorded at 1,000 Hz and is plotted with a 1,000-frame average.

bioRxiv preprint doi: https://doi.org/10.1101/265330; this version posted February 14, 2018. The copyright holder for this preprint (which was not certified by peer review) is the author/funder. All rights reserved. No reuse allowed without permission.

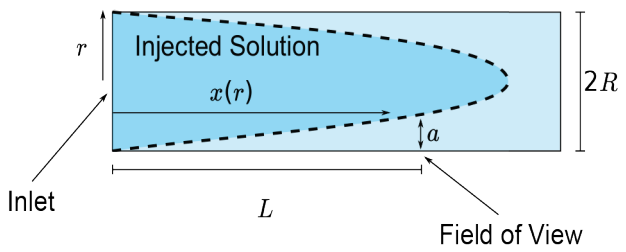

Supplementary Figure 11: **Model of the flow profile for the injected protein.** We model the flow chamber as a cylinder, as discussed in the Supplementary Notes. The dashed line represents the parabolic boundary between the injected protein solution and the solution that is already in the chamber.

bioRxiv preprint doi: https://doi.org/10.1101/265330; this version posted February 14, 2018. The copyright holder for this preprint (which was not certified by peer review) is the author/funder. All rights reserved. No reuse allowed without permission.

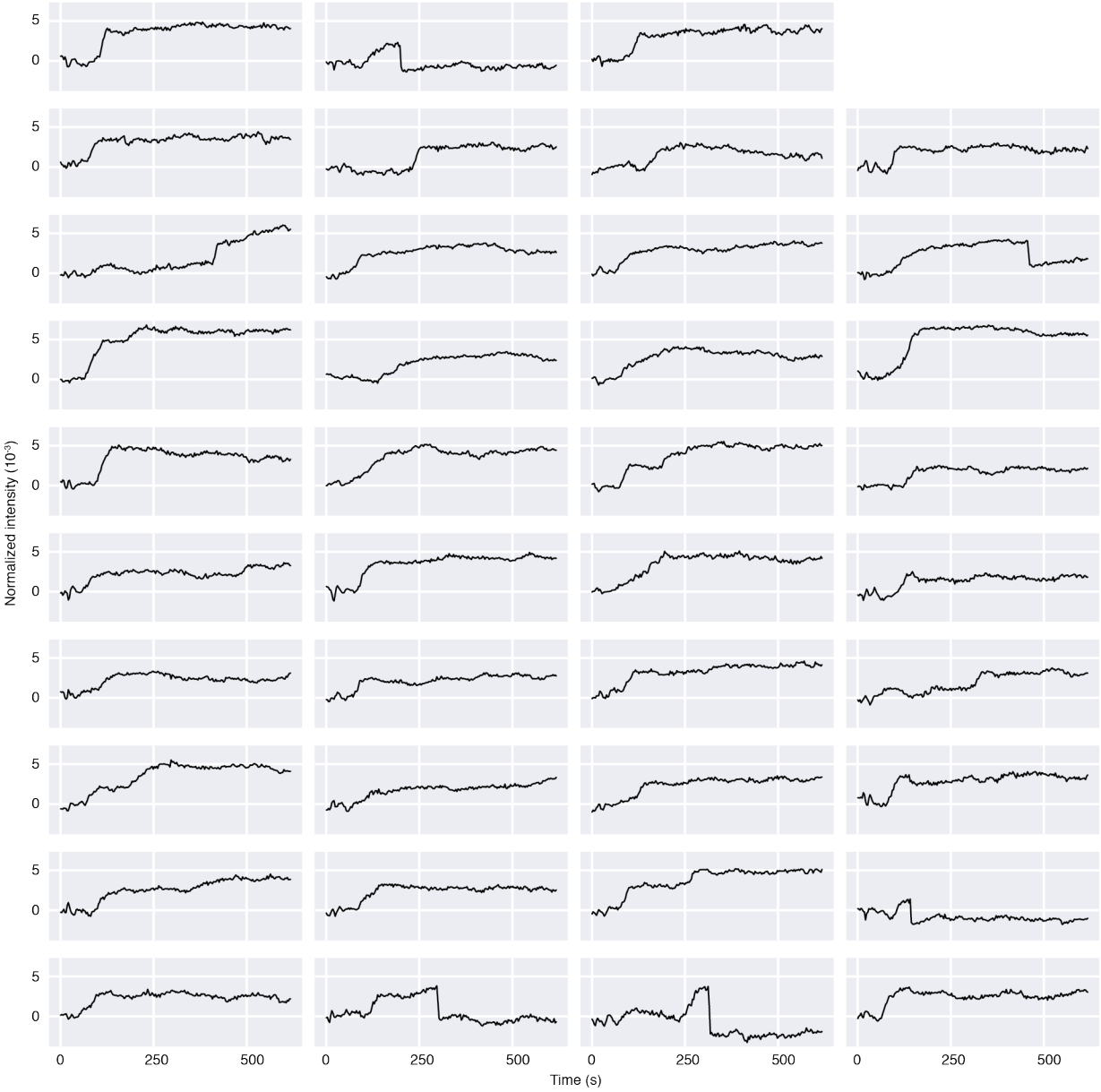

Supplementary Figure 12: **A control experiment with 2 μM of coat-protein dimers and lower imaging-laser intensity**. In this assembly experiment, we use light that is 10-fold less intense than in the experiment described in the main text, so that we can determine whether the imaging beam affects the assembly process. A full description of this experiment is in the Supplementary Notes. The results are similar to those of the 2 μM experiments shown in Figure 4c and in Supplementary Figures 9 and 13. The growth curves are measured from the data shown in Supplementary Movie 4. The data is recorded at 100 Hz and is plotted with a 300-frame average.

bioRxiv preprint doi: https://doi.org/10.1101/265330; this version posted February 14, 2018. The copyright holder for this preprint (which was not certified by peer review) is the author/funder. All rights reserved. No reuse allowed without permission.

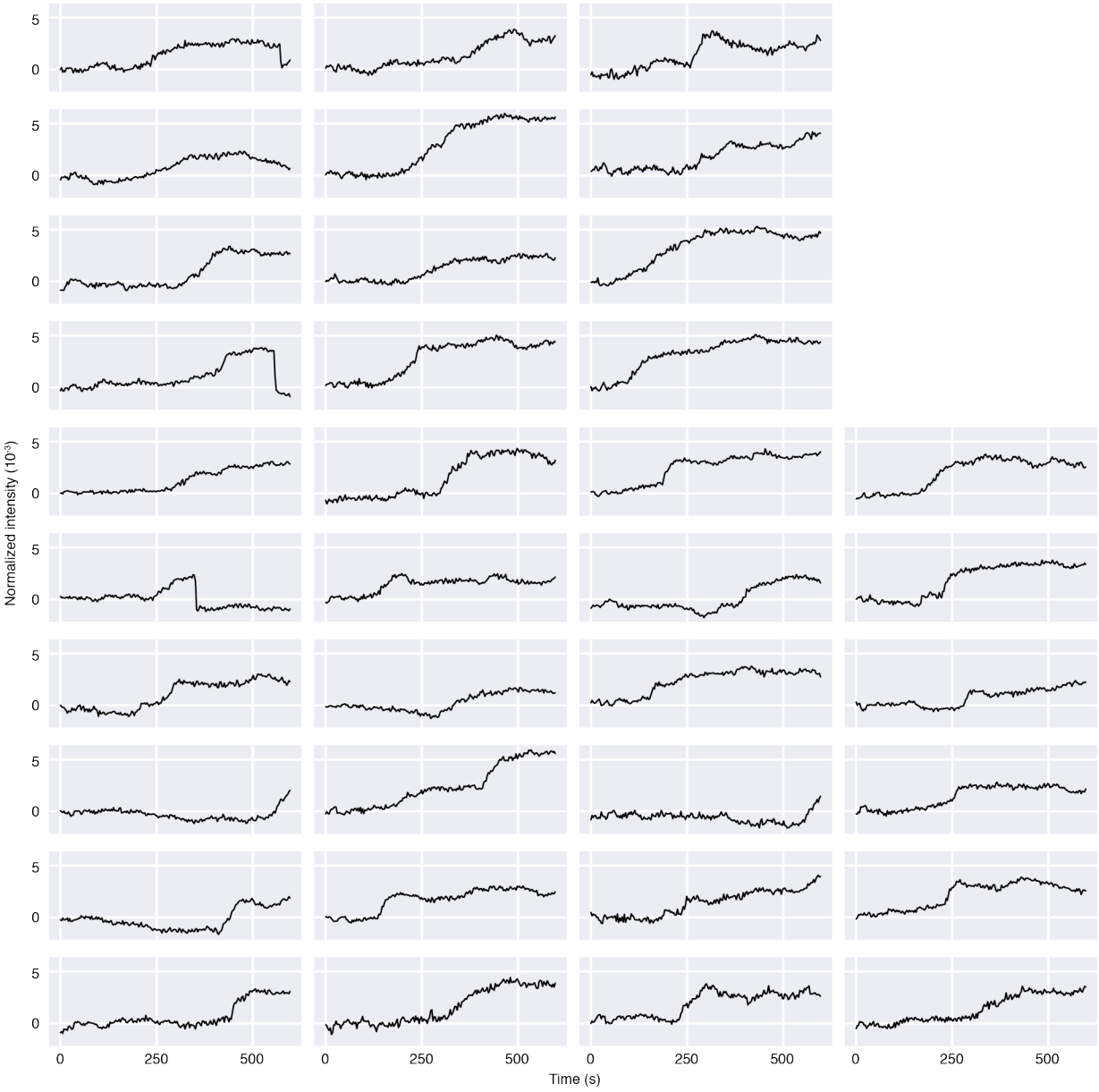

Supplementary Figure 13: **A duplicate control experiment with 2 μM of coat-protein dimers and lower imaging-laser intensity**. This experiment was performed identically to the one described in Supplementary Figure **12**. The growth curves are measured from the data shown in Supplementary Movie 5. The data is recorded at 100 Hz and is plotted with a 300-frame average.

bioRxiv preprint doi: https://doi.org/10.1101/265330; this version posted February 14, 2018. The copyright holder for this preprint (which was not certified by peer review) is the author/funder. All rights reserved. No reuse allowed without permission.

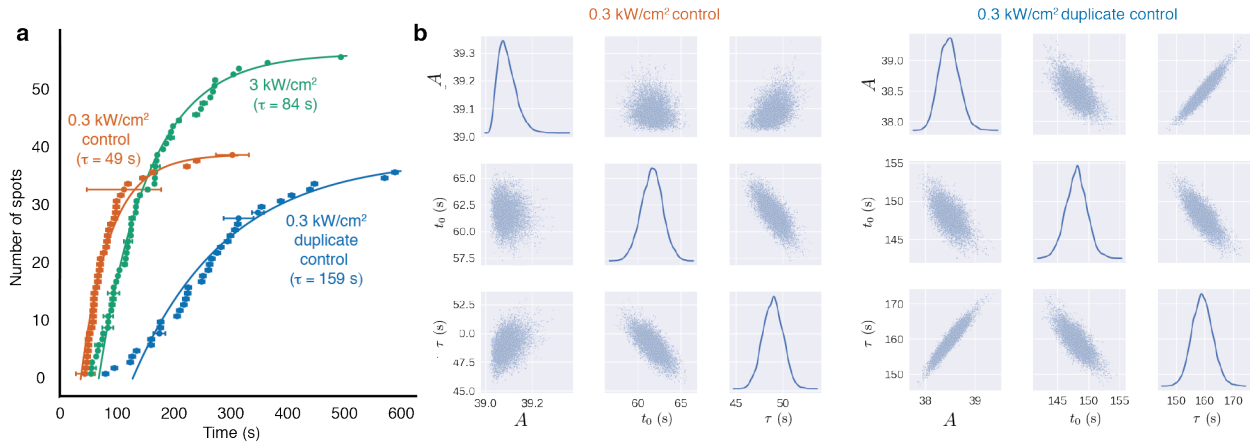

Supplementary Figure 14: **Comparison of the nucleation kinetics for three independent assembly experiments performed with 2 μM of coat-protein dimers**. (a) To test if the intensity of the illumination beam affects the assembly process, we compare the cumulative distribution of wait times for the experiment described in Figure 4 (replotted here in green) to that of a set of duplicate control experiments described in Supplementary Figures 12 (orange) and 13 (blue), where the illumination intensity is an order of magnitude smaller. The difference in the characteristic times for the duplicate control experiments is larger than the difference between the higher illumination intensity experiment and either of the controls, suggesting that other experimental uncertainties, such as differences in the injected protein concentration or in the flow profile within the imaging chamber, have a larger affect on the kinetics than the illumination intensity. The error bars represent the uncertainty in the time measurement, as described in the Supplementary Notes. (b) The posterior probability distributions of parameter values obtained by fitting the data from the control experiments. The plots along the diagonal show kernel density estimates of the fully marginalized posterior distributions of each parameter, while the off-diagonal plots show the joint distributions.

bioRxiv preprint doi: https://doi.org/10.1101/265330; this version posted February 14, 2018. The copyright holder for this preprint (which was not certified by peer review) is the author/funder. All rights reserved. No reuse allowed without permission.

Supplementary Note: Control assembly experiment with lower illumination intensity and 2 μM protein

To test whether the intensity of the incident beam affects the assembly process, we perform a set of duplicate control experiments with 2 μM of coat-protein dimers and a light intensity that is 10-fold smaller (approximately 0.3 kW/cm^2). The results of this experiment are shown in Supplementary Figures **12**, **13**, and **14**, and in Supplementary Movies 4 and 5.

The results of the control experiments are similar to those of the higher-intensity experiment presented in Figure **4** of the main text and Supplementary Figure **9**. Again, different assemblies appear after different wait times. The cumulative distribution function of the wait times is well-fit by the same exponential function but with $t_0 = 62 \pm 1$ s, $A = 39.08\ ^{+0.04}_{-0.03}$, and $\tau = 49 \pm 1$ s for the first control experiment of the duplicate set, and $t_0 = 148 \pm 2$ s, $A = 38.5 \pm 0.2$, and $\tau = 159 \pm 4$ s for the second control experiment (Supplementary Figure **14**). Also, about half of the assemblies (19 of 39) grow to intensities consistent with that of a full capsid, 5 grow to smaller intensities, and 15 grow to larger intensities in the first control experiment (Supplementary Figure **12**), while about half of the assemblies (17 of 36) grow to intensities consistent with that of a full capsid, 10 grow to smaller intensities, and 9 grow to larger intensities in the second experiment (Supplementary Figure **13**). These fractions are similar to that observed in the 2 μM experiment presented in the main text.

The results of the control experiments indicate that the incident light does not qualitatively affect the assembly process. The observed growth curves and distribution of wait times are consistent with those expected from a nucleation-and-growth process. Moreover, because the difference between identically performed low-intensity control experiments is larger than those between the high-intensity experiment and either of the controls, we conclude that other factors, such as differences in the concentration of protein, are responsible for the variation. Indeed, the variation in both the time constants, τ, and the delay times,

bioRxiv preprint doi: https://doi.org/10.1101/265330; this version posted February 14, 2018. The copyright holder for this preprint (which was not certified by peer review) is the author/funder. All rights reserved. No reuse allowed without permission.

t_0, of the exponential fits between different experiments is not unexpected, given the strong dependence of the wait times on concentration. At 1 μM protein concentration, all the wait times are longer than the 600 s duration of the experiment (Supplementary Figure 7), so that even a slight difference in the protein concentration introduced during the 2 μM experiments could cause the 110 second spread between the measured time constants and the 86 second spread in the delay times.

Supplementary Note: Procedure for fitting the cumulative distribution function

The cumulative distribution functions of the wait times before assembly (Figure 4b of the main text and Supplementary Figures 14) are measured as follows. Each wait time is defined as the time at which an assembly growth curve reaches an intensity of 0.001. To measure this time, we smooth each growth curve using a 1,000-frame moving average. The first time that the smoothed curve reaches an intensity greater than 0.001 is called t_1, and the last time that the smoothed curve has an intensity less than 0.001 is called t_2 (ignoring any late detachment events or decreases in intensity). The wait time is then determined as $t_{\text{wait}} = (t_1 + t_2)/2$. To estimate the uncertainty in each wait time, we calculate the half width of the moving average window and $(t_2 - t_1)/2$, and we take the greater of the two. The cumulative distribution function of wait times is obtained by sorting the measured values of t_{wait}.

The cumulative distribution of wait times is then fit to the exponential function $n(t) = A\left(1 - \exp\left[-(t - t_0)/\tau\right]\right)$ using a Bayesian parameter-estimation framework. A uniform, unbounded prior is used for all parameters. The exponential function is first inverted, yielding

$$t(n) = t_0 - \tau \ln\left(1 - n/A\right), \tag{1}$$

where the fit parameters are t_0, A, and τ. The posterior probability distribution $p(t_0, A, \tau \mid D_{\text{CDF}}, M)$, where D_{CDF} is the observed cumulative distribution function and M is the model

bioRxiv preprint doi: https://doi.org/10.1101/265330; this version posted February 14, 2018. The copyright holder for this preprint (which was not certified by peer review) is the author/funder. All rights reserved. No reuse allowed without permission.

(Equation (1)), is then sampled using an affine-invariant ensemble Markov-chain Monte Carlo sampler[57] with 50 walkers that take 500 steps each. The walkers are initially distributed in a narrow Gaussian around the peak of the posterior probability density function. The position of the peak is calculated from a least-squares fit to $t(n)$. The walkers reach an equilibrium distribution after approximately 150 steps. Pair plots of the positions of the walkers on every step after the burn-in are shown in Supplementary Figures **8** and **14**, along with the marginal distributions for each fit parameter. The best-fit parameters reported in the text are taken as the 50th percentile of the marginal distributions, and the reported uncertainties represent the 16th and the 84th percentile.

Supplementary Note: Identifying assemblies in the interferometric-scattering movies

To identify assemblies, we manually locate the centers of all dark spots that appear and are between 1 and 4 pixels across in each processed interferometric scattering movie. We repeat this procedure multiple times using different frames for the background subtraction to ensure that no dark spots are missed. For each of these spots, we measure intensity as a function of time.

Then we determine which spots likely represent the assembly of coat proteins around a single RNA molecule. We reject spots using the following criteria: (1) The spot instantaneously appears in the movie, indicating that it is from a particle that has adsorbed to the coverslip; (2) the spot is near the gold particle used for active stabilization or near a defect on the coverslip that has comparable intensity (greater than 0.1); (3) the spot is near a particle that adsorbs to or desorbs from the coverslip, such that its intensity is altered by the particle; (4) the spot is so close to another spot that the interference fringes of the two spots overlap; (5) the spot is near the edge of the field of view. Below we describe how each of the criteria are applied.

The spots from particles that adsorb to the coverslip are easily identified because they

bioRxiv preprint doi: https://doi.org/10.1101/265330; this version posted February 14, 2018. The copyright holder for this preprint (which was not certified by peer review) is the author/funder. All rights reserved. No reuse allowed without permission.

appear instantaneously in one frame of the movie instead of gradually appearing over the course of many frames. In some cases, such particles can be seen approaching the coverslip before adsorption.

Spots within 8 pixels of the gold particle used for active stabilization or a bright defect on the coverslip are rejected. There are typically fewer than 2 defects on the coverslip in a given field of view. The spots that grow near the gold particle or defect are not analyzed because they may be due to growth that is occurring on the gold particle or defect instead of on the RNA. Furthermore, the in-plane active stabilization keeps the coverslip position constant to within only a few nanometers, and when particles as bright as the gold particles move by a few nanometers they produce intensity changes that are similar to, or larger than the intensity of an MS2 capsid. These intensity changes affect the measured intensity of any nearby assemblies.

To determine if a spot is near a particle that adsorbs to or desorbs from the coverslip, we check if the interference fringes of an absorbing or desorbing particle overlap with the spot at any point during the movie. If it does, we examine its intensity as a function of time to check if there is an abrupt change in intensity that occurs on the same frame as the adsorption or desorption event. If the abrupt change in intensity is greater than 0.0003 (10% of the intensity of a capsid), we reject the spot for analysis. By not analyzing these spots we avoid misinterpreting intensity changes that are due to the adsorption or desorption event as features of the assembly kinetics.

A spot is determined to be too close to another spot if their centers are within 4 pixels of each other. If two spots are closer than this distance, their interference fringes overlap, and the measured intensity of each will depend on the intensity of the other.

Similarly, we do not analyze any spot with a center that is within 4 pixels of the edge of the field of view. We do not analyze these spots because the interference patterns for the spot are not fully visible, and we cannot determine if there are particles beyond the edge of the field of view that affect the spot's intensity.

bioRxiv preprint doi: https://doi.org/10.1101/265330; this version posted February 14, 2018. The copyright holder for this preprint (which was not certified by peer review) is the author/funder. All rights reserved. No reuse allowed without permission.

Supplementary Note: Estimating the time it takes for protein to reach the surface-bound RNA

Here we estimate how long it takes MS2 coat-protein dimers to reach the surface-bound RNA molecules after the protein is pumped into the imaging chamber. This time scale is set by the rate of diffusion and the distance betwen the protein and coverglass when it is first introduced.

We first model how fluid is introduced into the imaging chamber. Downstream of the inlet cup, the flow cell contains a cylindrical inlet chamber (1 mm diameter, 3 mm long), which is followed by the imaging chamber (0.75 mm tall, 1.0 mm wide, and 4.6 mm long) that contains our field of view. The field of view is in the center of the bottom surface of the imaging chamber. To simplify our calculations, we assume that the flow cell consists of a single cylindrical chamber with a radius of $R = 0.375$ mm and that our field of view is $L = 9.3$ mm from the entrance to the cylinder. The diameter of the cylinder is chosen to match the height of the imaging chamber, and the length L is chosen so that the volume $\pi L R^2$ is the same as the total volume in the actual inlet and imaging chambers upstream of the field of view.

We assume a no-slip boundary condition, such that the flow profile in the model cylindrical chamber is laminar and parabolic.[32] In our experiments, we inject $V = 10$ μL of fluid over 20 s, so that the average flow velocity is approximately 0.5 mm/s, yielding a Reynolds number of 0.5, which justifies the laminar assumption. We further assume that the diffusion of protein across the chamber is negligible over the duration of the pumping, so that the parabolic front that separates the new protein solution from the old buffer solution is sharply defined. Indeed, the time it takes for a MS2 coat-protein dimer (hydrodynamic radius 2.5 nm[11] with diffusion coefficient, $D = 90$ μm^2/s) to diffuse across the cylinder radius is approximately 1600 s, much longer than the pumping duration. The shape of the parabolic boundary is described by $x(r) = (2V/\pi R^2)\,(1 - (r/R)^2)$, where r is the radial coordinate of the cylinder, and $x(r)$ is the distance down the cylinder from the end where the protein is in-

bioRxiv preprint doi: https://doi.org/10.1101/265330; this version posted February 14, 2018. The copyright holder for this preprint (which was not certified by peer review) is the author/funder. All rights reserved. No reuse allowed without permission.

jected (see Supplementary Figure 11). Note that in the center of the cylinder, $x(r = 0) \approx 45$ mm. Thus, the tip of the parabola following a pump of V = 10 μL extends well beyond the field of view. Above the field of view, the distance from the parabolic boundary to the surface is $a = R(1 - \sqrt{1 - \pi R^2 L/2V}) \approx 40$ μm. This is the distance that the protein must diffuse to reach the surface-bound RNA.

To experimentally determine the distance from the parabolic boundary to the surface just after the pump, we use a bright-field microscope (Eclipse Ti, Nikon) and tracer particles (1 μm sulfate-latex, Invitrogen). For this experiment we fill the flow cell with water, position our field of view in the center of the imaging chamber, inject a solution of tracer particles (0.08% w/v in water), and measure the distance of the tracer particles from the coverslip immediately after the injection. We find that there is a well-defined boundary between the solutions with and without particles, and that this boundary is a = 20–50 μm above the coverslip, depending on the pump and flow cell used. This distance agrees well with the distance calculated above (40 μm).

With this length scale and the diffusion coefficient, we can calculate the time it takes proteins to diffuse to the surface, $t_{\mathrm{D}} = a^2/D$. More specifically, at a distance a from the protein solution, t_{D} is the time it takes for the concentration of proteins to reach approximately half of the injected concentration. We find that, for a 20–50 μm distance, t_{D} = 5–30 s.

This timescale agrees with the measured delay time that precedes assembly in experiments performed with 2 μM protein. For our assembly experiments, we stop the injection pump 24 s after the time-series begins, so when we introduce 2 μM of coat-protein dimers, the concentration of protein at the surface should reach 1 μM about 30 to 55 s after the beginning of the time-series. Since we determine that 1 μM of protein is too low to initiate assembly on our experimental time scale (Supplementary Figure 7), we do not expect assembly to occur during the first 30 to 55 s of the time-series. Consistent with this expectation, the first assemblies appear between 69 to 104 s into the time-series, depending on the experiment (Supplementary Figure 14). These time scales correspond to when the concentration of

bioRxiv preprint doi: https://doi.org/10.1101/265330; this version posted February 14, 2018. The copyright holder for this preprint (which was not certified by peer review) is the author/funder. All rights reserved. No reuse allowed without permission.

protein at the surface is expected to be greater than 1 μM.

Supplementary Note: Buffer recipes

Assembly buffer: 42 mM Tris-HCl, pH 7.5; 84 mM NaCl; 3 mM acetic acid; 1 mM EDTA

Hybridization buffer: 50 mM Tris-HCl, pH 7.0; 200 mM NaCl; 1 mM EDTA

TAE buffer: 40 mM Tris-acetic acid, pH 8.3; 1 mM EDTA

TNE buffer: 50 mM Tris-HCl, pH 7.5; 100 mM NaCl; 1 mM EDTA

TE buffer: 10 mM Tris-HCl, pH 7.5; 1 mM EDTA

Captions for supplementary movies

Supplementary Movie 1: The time-series of images from the assembly experiment using 1 μM of protein (Supplementary Figure **7**). The time-series is recorded at 100 Hz, is shown with a 300-frame average, and is sped up by a factor of 100 for playback. The field of view is 14 μm on each side. The illumination beam is blocked for a short time approximately halfway through the movie, just before 2 μM of protein is added. In the first half of the movie, where 1 μM of protein is in the imaging chamber, a few particles are seen adsorbing to the coverslip, but no assemblies are seen growing on the coverslip. In the second half of the movie, where 2 μM of protein is in the imaging chamber, a number of assemblies are seen growing on the coverslip.

Supplementary Movie 2: The time-series of images from the assembly experiment using 2 μM of protein (Figure 4, Supplementary Figures **9** and **10**a). The time-series is recorded at 1,000 Hz, is shown with a 1,000 frame average, and is sped up by a factor of 100 for playback. The field of view is 9.8 μm on each side.

bioRxiv preprint doi: https://doi.org/10.1101/265330; this version posted February 14, 2018. The copyright holder for this preprint (which was not certified by peer review) is the author/funder. All rights reserved. No reuse allowed without permission.

Supplementary Movie 3: The time-series of images from the control experiment using 2 μM of protein with no RNA on the coverslip (Supplementary Figure **10**b). The time-series is recorded at 1,000 Hz, is shown with a 1,000 frame average, and is sped up by a factor of 100 for playback. The field of view is 9.8 μm on each side.

Supplementary Movie 4: The time-series of images from the first of two assembly experiments using 2 μM of protein with a low illumination intensity (Supplementary Figure **12**). The time-series is recorded at 100 Hz, is shown with a 300-frame average, and is sped up by a factor of 100 for playback. The field of view is 14 μm on each side. The number of surface-bound RNA strands is exceptionally high in this movie. A large particle adsorbs to the coverslip around halfway through the movie, and a second large particle binds transiently in the upper-left corner.

Supplementary Movie 5: The time-series of images from the second assembly experiment using 2 μM of protein with a low illumination intensity (Supplementary Figure **13**). The time-series is recorded at 100 Hz, is shown with a 300-frame average, and is sped up by a factor of 100 for playback. The field of view is 14 μm on each side. A few large particles adsorb to the coverslip in the second half of the movie.